

A local Fourier analysis of additive Vanka relaxation for the Stokes equations

Patrick E. Farrell¹ | Yunhui He^{*2} | Scott P. MacLachlan²

¹Mathematical Institute, University of Oxford, UK

²Department of Mathematics and Statistics, Memorial University of Newfoundland, St. John's, NL, Canada

Correspondence

*Yunhui He, Department of Mathematics and Statistics, Memorial University of Newfoundland, St. John's, NL, A1C 5S7, Canada. Email: yunhui.he@mun.ca

Summary

Multigrid methods are popular solution algorithms for many discretized PDEs, either as standalone iterative solvers or as preconditioners, due to their high efficiency. However, the choice and optimization of multigrid components such as relaxation schemes and grid-transfer operators is crucial to the design of optimally efficient algorithms. It is well-known that local Fourier analysis (LFA) is a useful tool to predict and analyze the performance of these components. In this paper, we develop a local Fourier analysis of monolithic multigrid methods based on additive Vanka relaxation schemes for mixed finite-element discretizations of the Stokes equations. The analysis offers insight into the choice of “patches” for the Vanka relaxation, revealing that smaller patches offer more effective convergence per floating point operation. Parameters that minimize the two-grid convergence factor are proposed and numerical experiments are presented to validate the LFA predictions.

KEYWORDS:

Monolithic Multigrid, Stokes Equations, Additive Vanka, Local Fourier Analysis, Triangular Grids

1 | INTRODUCTION

Saddle-point problems are ubiquitous in applied mathematics.¹ Their importance motivates the development of effective parallel solvers. Block preconditioners and monolithic multigrid methods are established approaches for solving linear (or linearized) saddle-point problems. Block preconditioning is highly effective when the Schur complement of the system is well understood; for the Stokes equations, the Schur complement is spectrally equivalent to a weighted mass matrix, forming the basis for efficient solvers that use multigrid for the viscous term.^{2,3} Monolithic methods that apply multigrid to the entire system can also offer superb efficiency if an appropriate relaxation can be devised. For example, Adler et al.⁴ proposed a monolithic multigrid method with Braess-Sarazin relaxation for the Stokes equations that provided the fastest time to solution when compared with several block preconditioners and other monolithic multigrid methods. While many block preconditioners have been successfully employed in (massively) parallel computing environments^{5,6}, the same cannot be said for monolithic multigrid, whose parallelization was largely absent from the literature until recently⁷⁻⁹.

Common approaches to multigrid relaxation for coupled systems are distributive relaxation¹⁰ (which relies on continuum commutativity that may not hold at the discrete level), Braess-Sarazin relaxation,^{11,12} and Vanka relaxation.¹³ Based on distributive relaxation, Wang and Chen¹⁴ developed a least squares commutator distributive Gauss-Seidel relaxation for the Stokes equations. Furthermore, this technique has been extended to the Oseen problem by Chen et al.¹⁵ Braess-Sarazin relaxation is known to be highly efficient, and has been applied to nematic liquid crystals,¹⁶ magnetohydrodynamics,¹² and other coupled systems. Considering parallel computation, recently, He and MacLachlan presented a local Fourier analysis (LFA) for

both distributive weighted Jacobi and Braess–Sarazin relaxations for the Stokes equations discretized by the Marker-and-Cell finite-difference scheme¹⁷ and by mixed finite-element methods,¹⁸ showing the power of LFA for designing efficient algorithms.

Vanka-type relaxation has been used in many contexts, such as for the Navier–Stokes equations,^{13, 19} and extended to Vanka-like schemes for other problems or to improve performance.^{4, 7, 12, 20–22} However, Vanka relaxation is typically considered in its multiplicative variant. This seems overly constraining, particularly in comparison to Braess–Sarazin relaxation, which can naturally be done in additive form.^{17, 18} While multiplicative Vanka relaxation is very efficient, the cost is also high and it is not suitable for parallel computation. We therefore consider additive variants of Vanka-type relaxation in this work.

There are two challenging choices to be made for Vanka relaxation, which are observed to be more critical in the additive setting. First, many choices are possible for the underlying patches within the overlapping Schwarz framework. While we would naturally choose small patches for efficiency or large patches for effectiveness, no general results are known. Secondly, relaxation weights play an important role in ensuring best possible performance of the multigrid algorithm, particularly for additive methods. Thus, there is a need for analysis to inform the algorithmic choices, and LFA seems well-suited. LFA has already been applied to Vanka relaxation in the multiplicative^{23–27} and multicoloured²⁸ contexts; here, in contrast, we aim to develop LFA for additive schemes and use it to drive parameter choices in practical experiments for the Stokes equations. To our knowledge, this is the first time that LFA has been applied to additive overlapping Vanka relaxation.

We consider the Stokes equations as a model problem, with both $P_2 - P_1$ and $Q_2 - Q_1$ discretizations. We propose two constructions of the patches for Vanka relaxation, and two approaches to determining relaxation weights. It is shown that using weighting based on patch geometry outperforms a simpler approach. We also find that using small patches with low-degree Chebyshev iterations leads to more efficient multigrid algorithms than with bigger patches or more relaxation steps per iteration, when cost per sweep is accounted for. Although there are no general rules to facilitate the choice of patches or weights, taking advantage of LFA, we can optimize the weights. For validation, our numerical tests are implemented using Firedrake²⁹ and PETSc.^{30, 31} Numerical experiments are shown to match the LFA predictions for both periodic and Dirichlet boundary conditions. We observe that performance is less sensitive to overestimates of the weights for relaxation schemes considered here, which has also been seen in other works.^{4, 12} Last but not least, we compare the cost and performance of relaxation schemes considered here.

This paper is organized as follows. In Section 2, we introduce the $P_2 - P_1$ and $Q_2 - Q_1$ discretizations considered here and the multigrid framework with additive Vanka relaxation for the Stokes equations. In Section 3, we first give an introduction to LFA, then propose an LFA for the Stokes equations with additive Vanka relaxation. In Section 4, two types of overlapping patches are considered, and we validate the LFA predictions with two-grid experiments. Conclusions and remarks are given in Section 5.

2 | DISCRETIZATION AND SOLUTION OF THE STOKES EQUATIONS

2.1 | Mixed finite-element discretization of the Stokes equations

In this paper, we consider the Stokes equations,

$$\begin{aligned} -\Delta \vec{u} + \nabla p &= \vec{f}, \\ -\nabla \cdot \vec{u} &= 0, \end{aligned} \tag{1}$$

where \vec{u} is the velocity vector, p is the scalar pressure of a viscous fluid, and \vec{f} represents a (known) forcing term, together with suitable boundary conditions.

The natural finite-element approximation of Problem (1) when coupled with Dirichlet boundary conditions on \vec{u} on some portion of the domain boundary is: Find $\vec{u}_h \in \mathcal{X}^h$ and $p_h \in \mathcal{H}^h$ such that

$$a(\vec{u}_h, \vec{v}_h) + b(p_h, \vec{v}_h) + b(q_h, \vec{u}_h) = g(\vec{v}_h), \text{ for all } \vec{v}_h \in \mathcal{X}_0^h \text{ and } q_h \in \mathcal{H}^h, \tag{2}$$

where

$$\begin{aligned} a(\vec{u}_h, \vec{v}_h) &= \int_{\Omega} \nabla \vec{u}_h : \nabla \vec{v}_h, \quad b(p_h, \vec{v}_h) = - \int_{\Omega} p_h \nabla \cdot \vec{v}_h, \\ g(\vec{v}_h) &= \int_{\Omega} \vec{f}_h \cdot \vec{v}_h, \end{aligned}$$

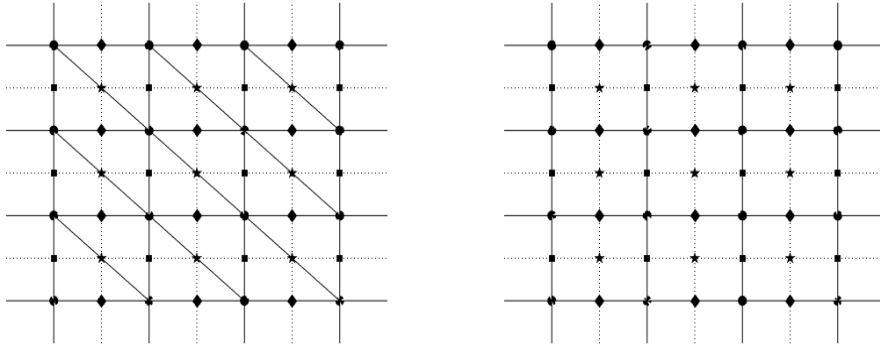


FIGURE 1 Meshes and finite-element degrees of freedom (see definitions in (7)), with \bullet denoting N -type and P_1/Q_1 DoFs, \blacklozenge denoting X -type DoFs, \blacksquare denoting Y -type DoFs, and \star denoting C -type DoFs. At left, $P_2 - P_1$ discretization on triangles. At right, $Q_2 - Q_1$ discretization on quadrilaterals.

and $\mathcal{X}^h \subset H^1(\Omega)$, $\mathcal{H}^h \subset L_2(\Omega)$ are finite-element spaces. Here, \mathcal{X}_0^h satisfies homogeneous Dirichlet boundary conditions in place of any non-homogenous essential boundary conditions on \mathcal{X}^h . Problem (2) has a unique solution only when \mathcal{X}^h and \mathcal{H}^h satisfy an inf-sup condition.^{32–35}

Remark 1. If considering an outflow boundary condition, the stress-divergence form of the viscous term should be used instead³⁶. The framework for LFA presented in this paper can easily be extended to this situation; however, the two-grid error-propagation operator (and its LFA representation) depends directly on the stencils of the discretized operators. Thus, considering this form instead of (2) may affect the optimal choice of parameters and the resulting performance of the two-grid method.

Here, we consider two types of stable finite-element methods for the Stokes equations. First, we consider the stable mixed approximation for structured meshes of triangular elements using continuous quadratic approximations for the velocity components and continuous linear approximations for the pressure, the $P_2 - P_1$ approximation.³² Secondly, we consider the stable approximation for rectangular meshes, using continuous biquadratic approximations for the velocity components and continuous bilinear approximations for the pressure, the $Q_2 - Q_1$ (Taylor–Hood) approximation. Both approximations can be represented via nodal basis functions, as illustrated in Figure 1.

Discretizations of (1) typically lead to linear systems of the form

$$Ky = \begin{pmatrix} A & B^T \\ B & -C \end{pmatrix} \begin{pmatrix} u \\ p \end{pmatrix} = \begin{pmatrix} f \\ 0 \end{pmatrix} = b, \quad (3)$$

where A corresponds to the discretized vector Laplacian, and B is the negative of the discrete divergence operator. If the discretization is naturally unstable, then $C \neq 0$ is the stabilization matrix, otherwise $C = 0$.³² For the stable $P_2 - P_1$ and $Q_2 - Q_1$ finite-element discretizations considered here, we take $C = 0$.

2.2 | Monolithic multigrid for the Stokes equations

System (3) is of saddle–point type. Here, we consider the numerical solution of (3) using a monolithic multigrid iteration applied to the full system collectively with a suitable (coupled) relaxation method. As is typical for geometric multigrid, a relaxation technique is employed to quickly damp all oscillatory components of the error. Subsequently, a coarse-grid correction scheme, where a projected problem is solved on a coarser grid and the solution is interpolated as an error correction to the fine-grid approximation, is used to damp the smooth components of the error. In order to describe monolithic multigrid, assume we have two meshes, with fine-grid meshsize h and coarse-grid meshsize H (often, $H = 2h$, by doubling the meshsize in each spatial direction).

For a general nonsingular linear system, $K_h u_h = b_h$, we consider a stationary iteration as the relaxation scheme. Given an approximation, M_h , to K_h that can be inverted easily, the approximate solution is updated via the iteration

$$u_h^{j+1} = (I - M_h^{-1} K_h) u_h^j + M_h^{-1} b_h. \quad (4)$$

The matrix $S_h := I - M_h^{-1}K_h$ is the error propagation operator for relaxation. With restriction and interpolation operators, R_h and P_h , respectively, and coarse-grid matrix K_H , the two-grid error propagation operator corresponding to the relaxation scheme in (4) can be written as

$$E_h = S_h^{v_2} (I - P_h K_H^{-1} R_h K_h) S_h^{v_1}, \quad (5)$$

where $I - P_h K_H^{-1} R_h K_h$ is called the coarse-grid correction operator.

The Jacobi, Gauss-Seidel, and Richardson schemes are often used for relaxation, particularly for discretizations of scalar PDEs. For the restriction operator, R_h , there are many choices, which depend on the problem under consideration. Here, we focus on choices of R_h tied to the mesh and the particular discretization scheme used to generate K_h . The coarse-grid operator, K_H can be the Galerkin operator, $K_H = R_h K_h P_h$, or the natural redispertization operator (or any other choice). The interpolation operator, P_h , is usually taken to be the conjugate transpose of R_h , with scaling depending on the discretization scheme and the dimension of the considered problem. For more details on the choice of multigrid components, see^{37–39}.

If we solve the coarse-grid problem recursively by the two-grid method, then we obtain a multigrid method. Over the past decades, a variety of types of multigrid methods have been developed, including W , V , and F -cycles³⁸. In this paper, we focus on using additive Vanka-type relaxation in combination with a monolithic multigrid method to solve (3). This means that M_h is constructed by the Vanka approach, and updates both components of the solution to (3) at the same time in the relaxation scheme. Only two-grid schemes are considered.

2.2.1 | Overlapping Schwarz relaxation

Here, we present the multiplicative and additive Schwarz approaches to solve $K_h u_h = b_h$. Let the degrees of freedom (DoFs) of u_h be the set \mathfrak{S} , and $\mathfrak{S}_i, i = 1, 2, \dots, N$, be subsets of unknowns with $\mathfrak{S} = \bigcup_{i=1}^N \mathfrak{S}_i$. Let V_i be the restriction operator mapping from vectors over the set of all unknowns, \mathfrak{S} , to vectors whose unknowns consist of the DoFs in \mathfrak{S}_i . Then $K_i = V_i K_h V_i^T$ is the restriction of K_h to the i -th block of DoFs. Moreover, let $D_i = \text{diag}(d_1^i, d_2^i, \dots, d_{m_i}^i)$ for $i = 1, \dots, N$ be a diagonal weight matrix for each block i , where m_i is the dimension of K_i . Then, the multiplicative and additive Schwarz iterations are presented in Algorithm 1.

Algorithm 1

Multiplicative Schwarz iteration:

$u^{j,0} = u^{j-1,N}$. For $i = 1, \dots, N$,

$$K_i \delta u_i = V_i (b_h - K_h u^{j,i-1}),$$

and

$$u^{j,i} = u^{j,i-1} + V_i^T D_i \delta u_i.$$

Additive Schwarz iteration:

For $i = 1, \dots, N$,

$$K_i \delta u_i = V_i (b_h - K_h u^j),$$

and

$$u^{j+1} = u^j + \sum_{i=1}^N V_i^T D_i \delta u_i.$$

The error-propagation operator for the multiplicative Schwarz procedure can be written as

$$S_m = \prod_{i=1}^N (I - V_i^T D_i K_i^{-1} V_i K_h)$$

and, for the additive Schwarz procedure, it is

$$S_a = I - M_h^{-1} K_h,$$

where

$$M_h^{-1} = \sum_{i=1}^N V_i^T D_i K_i^{-1} V_i. \quad (6)$$

More details about this algebraic viewpoint on the multiplicative and additive Schwarz iterations can be found, for example, in the work of Saad.⁴⁰ Overlapping multiplicative Schwarz approaches have been used as the relaxation scheme for the Stokes equations,^{4, 7, 13, 20–24} which we refer to as multiplicative Vanka relaxation. Extending this, we will refer to such overlapping additive Schwarz approaches as additive Vanka relaxation. In this paper, we focus on using additive Vanka as a relaxation scheme within monolithic multigrid for the Stokes equations. Some key questions in doing this are

1. How should the subsets \mathfrak{S}_i be chosen?
2. How should D_i be chosen?

In what follows, we consider uniform meshes for the domain, $\Omega = [0, 1]^2$. We will use the pressure DoFs to “seed” the sets, \mathfrak{S}_i , so that (away from the boundary) all sets will have the same structure and size m . In this paper, we use local Fourier analysis to guide the choice of \mathfrak{S}_i and other aspects of the relaxation scheme.

3 | LOCAL FOURIER ANALYSIS

3.1 | Definitions and notations

We first introduce some terminology of LFA.^{37, 41} We consider the following two-dimensional infinite uniform grids, $\mathbf{G}_h = \bigcup_{j=1}^4 \mathbf{G}_h^j$, where

$$\mathbf{G}_h^j = \{ \mathbf{x}^j := (x_1^j, x_2^j) = (k_1, k_2)h + \delta^j, (k_1, k_2) \in \mathbb{Z}^2 \}, \quad (7)$$

with

$$\delta^j = \begin{cases} (0, 0) & \text{if } j = 1, \\ (h/2, 0) & \text{if } j = 2, \\ (0, h/2) & \text{if } j = 3, \\ (h/2, h/2) & \text{if } j = 4. \end{cases}$$

We refer to $\mathbf{G}_h^1, \mathbf{G}_h^2, \mathbf{G}_h^3$, and \mathbf{G}_h^4 as the N -, X -, Y -, and C -type points on the grid \mathbf{G}_h , respectively, see Figure 1. The coarse grids, \mathbf{G}_{2h}^j , are defined similarly. Note that in much of the literature, LFA is applied to discretizations on \mathbf{G}_h^1 . Here, we consider the more general case as needed for P_2 and Q_2 finite elements.

Let L_h be a scalar Toeplitz operator defined by its stencil acting on $l^2(\mathbf{G}_h^j)$ as follows,

$$L_h \hat{=} [s_\kappa]_h \ (\kappa = (\kappa_1, \kappa_2) \in \mathbf{V}); \quad L_h w_h(\mathbf{x}^j) = \sum_{\kappa \in \mathbf{V}} s_\kappa w_h(\mathbf{x}^j + \kappa h), \quad (8)$$

with constant coefficients $s_\kappa \in \mathbb{R}$ (or \mathbb{C}), where $w_h(\mathbf{x}^j)$ is a function in $l^2(\mathbf{G}_h^j)$. Here, $\mathbf{V} \subset \mathbb{Z}^2$ is a finite index set. Because L_h is formally diagonalized by the Fourier modes $\varphi(\theta, \mathbf{x}^j) = e^{i\theta \cdot \mathbf{x}^j/h} = e^{i\theta_1 x_1^j/h} e^{i\theta_2 x_2^j/h}$, where $\theta = (\theta_1, \theta_2)$ and $i^2 = -1$, we use $\varphi(\theta, \mathbf{x}^j)$ as a Fourier basis with $\theta \in \left[-\frac{\pi}{2}, \frac{3\pi}{2}\right)^2$ (or any pair of intervals with length 2π).

For smoothing and two-grid analysis, we have to distinguish high and low frequency components on \mathbf{G}_h^j with respect to \mathbf{G}_{2h}^j .³⁷

Note that for any $\theta' \in \left[-\frac{\pi}{2}, \frac{\pi}{2}\right)^2$,

$$\varphi(\theta, \mathbf{x}^j) = \varphi(\theta', \mathbf{x}^j) \text{ for } \mathbf{x}^j \in \mathbf{G}_{2h}^j, \quad (9)$$

if and only if $\theta = \theta' \pmod{\pi}$. This means that only those frequency components, $\varphi(\theta, \cdot)$, with $\theta \in \left[-\frac{\pi}{2}, \frac{\pi}{2}\right)^2$ are distinguishable on \mathbf{G}_{2h}^j . Thus, high and low frequencies for standard coarsening ($H = 2h$) are given by

$$\theta \in T^{\text{low}} = \left[-\frac{\pi}{2}, \frac{\pi}{2}\right)^2, \quad \theta \in T^{\text{high}} = \left[-\frac{\pi}{2}, \frac{3\pi}{2}\right)^2 \setminus \left[-\frac{\pi}{2}, \frac{\pi}{2}\right)^2.$$

Definition 1. We call $\tilde{L}_h(\theta) = \sum_{\kappa \in \mathbf{V}} s_\kappa e^{i\theta \cdot \kappa}$ the symbol of L_h .

Note that for all functions $\varphi(\theta, \mathbf{x}^j)$,

$$L_h \varphi(\theta, \mathbf{x}^j) = \tilde{L}_h(\theta) \varphi(\theta, \mathbf{x}^j).$$

For a relaxation scheme, represented by matrix M_h for operator L_h , the error-propagation operator for relaxation can be written as

$$S_h(\rho) = I - M_h^{-1}(\rho) L_h,$$

where \mathbf{p} represents parameters within M_h . A typical relaxation scheme often reduces high-frequency error components quickly, but is slow to reduce low-frequency errors. Thus, it is natural to define the smoothing factor as follows.

Definition 2. The error-propagation symbol, $\tilde{S}_h(\boldsymbol{\theta}, \mathbf{p})$, for relaxation scheme $S_h(\mathbf{p})$ on the infinite grid \mathbf{G}_h satisfies

$$S_h(\mathbf{p})\varphi(\boldsymbol{\theta}, \mathbf{x}) = \tilde{S}_h(\boldsymbol{\theta}, \mathbf{p})\varphi(\boldsymbol{\theta}, \mathbf{x}), \quad \boldsymbol{\theta} \in \left[-\frac{\pi}{2}, \frac{3\pi}{2}\right)^2,$$

for all $\varphi(\boldsymbol{\theta}, \mathbf{x})$, and the corresponding smoothing factor for $S_h(\mathbf{p})$ is given by

$$\mu_{\text{loc}} = \mu_{\text{loc}}(S_h(\mathbf{p})) = \max_{\boldsymbol{\theta} \in T^{\text{high}}} \left\{ \left| \tilde{S}_h(\boldsymbol{\theta}, \mathbf{p}) \right| \right\}.$$

In many cases, the LFA smoothing factor offers a good prediction of actual two-grid performance, and we can optimize the smoothing factor with respect to the parameters, \mathbf{p} , to obtain an efficient algorithm. However, this is generally not true for higher-order finite-element approximations.^{18, 24, 42} Thus, we next introduce two-grid LFA, which still offers good predictions of performance in this setting.

Remark 2. In many applications of LFA, we consider a system operator rather than the discretization of a scalar PDE, and S_h is a block smoother. However, the definition of symbol and smoothing factor presented here can be extended to a system easily. Details on these extensions will be presented in section 3.3.

3.2 | Two-grid LFA

In general, LFA smoothing analysis gives a good prediction for the actual multigrid performance, under the assumption that we have an “ideal” coarse-grid-correction operator that annihilates low-frequency error components and leaves high-frequency components unchanged. However, in our setting, this assumption about ideal coarse-grid correction (CGC) does not hold (due to the discretization⁴²), but the two-grid LFA convergence factor still offers useful predictions.

To apply LFA to the two-grid operator, (5), and calculate the two-grid convergence factor, we need to analyse how the operators K_h, P_h, R_h , and S_h act on the Fourier components $\varphi(\boldsymbol{\theta}, \mathbf{x}^j)$. From (9), we know that values of $\varphi(\boldsymbol{\theta}, \mathbf{x}^j)$ coincide on \mathbf{G}_{2h}^j for four values of $\boldsymbol{\theta}$, known as harmonic frequencies. Let

$$\begin{aligned} \boldsymbol{\alpha} &= (\alpha_1, \alpha_2) \in \{(0, 0), (1, 0), (0, 1), (1, 1)\}, \\ \boldsymbol{\theta}^\alpha &= (\theta_1^{\alpha_1}, \theta_2^{\alpha_2}) = \boldsymbol{\theta} + \pi \cdot \boldsymbol{\alpha}, \quad \boldsymbol{\theta} := \boldsymbol{\theta}^{00} \in T^{\text{low}}. \end{aligned}$$

For a given $\boldsymbol{\theta} \in T^{\text{low}}$, we define the four-dimensional harmonic space

$$\mathcal{F}(\boldsymbol{\theta}) = \text{span} \left\{ \varphi(\boldsymbol{\theta}^\alpha, \cdot) : \boldsymbol{\alpha} \in \{(0, 0), (1, 0), (0, 1), (1, 1)\} \right\}.$$

Under standard assumptions, the space $\mathcal{F}(\boldsymbol{\theta})$ is invariant under the two-grid operator E_h .^{37, 41} We use the ordering of $\boldsymbol{\alpha} = (0, 0), (1, 0), (0, 1), (1, 1)$ for the four harmonics in the following, although, as with any invariant subspace, the ordering of the basis elements is unimportant.

Inserting the representations of S_h, K_h, K_H, P_h, R_h into (5), we obtain the Fourier representation of two-grid error-propagation operator as

$$\tilde{E}_h(\boldsymbol{\theta}, p) = \tilde{S}_h^{v_2}(\boldsymbol{\theta}, p) (I - \tilde{P}_h(\boldsymbol{\theta}) (\tilde{K}_H(2\boldsymbol{\theta}))^{-1} \tilde{R}_h(\boldsymbol{\theta}) \tilde{K}_h(\boldsymbol{\theta})) \tilde{S}_h^{v_1}(\boldsymbol{\theta}, p),$$

where

$$\begin{aligned} \tilde{K}_h(\boldsymbol{\theta}) &= \text{diag} \left\{ \tilde{K}_h(\boldsymbol{\theta}^{00}), \tilde{K}_h(\boldsymbol{\theta}^{10}), \tilde{K}_h(\boldsymbol{\theta}^{01}), \tilde{K}_h(\boldsymbol{\theta}^{11}) \right\}, \\ \tilde{S}_h(\boldsymbol{\theta}, p) &= \text{diag} \left\{ \tilde{S}_h(\boldsymbol{\theta}^{00}, p), \tilde{S}_h(\boldsymbol{\theta}^{10}, p), \tilde{S}_h(\boldsymbol{\theta}^{01}, p), \tilde{S}_h(\boldsymbol{\theta}^{11}, p) \right\}, \\ \tilde{R}_h(\boldsymbol{\theta}) &= \left(\tilde{R}_h(\boldsymbol{\theta}^{00}), \tilde{R}_h(\boldsymbol{\theta}^{10}), \tilde{R}_h(\boldsymbol{\theta}^{01}), \tilde{R}_h(\boldsymbol{\theta}^{11}) \right), \\ \tilde{P}_h(\boldsymbol{\theta}) &= \left(\tilde{P}_h(\boldsymbol{\theta}^{00}); \tilde{P}_h(\boldsymbol{\theta}^{10}); \tilde{P}_h(\boldsymbol{\theta}^{01}); \tilde{P}_h(\boldsymbol{\theta}^{11}) \right), \end{aligned}$$

in which $\text{diag}\{T_1, T_2, T_3, T_4\}$ stands for the block diagonal matrix with diagonal blocks, T_1, T_2, T_3 , and T_4 .

Definition 3. The asymptotic two-grid convergence factor, ρ_{asp} , is defined as

$$\rho_{\text{asp}} = \sup \left\{ \rho(\tilde{E}_h(\boldsymbol{\theta}, p)) : \boldsymbol{\theta} \in T^{\text{low}} \right\}. \quad (10)$$

In practical use, we typically consider a discrete form of ρ_{asp} , denoted by ρ , resulting from sampling ρ_{asp} over only a finite set of frequencies. In many cases, ρ provides a sharp prediction of actual two-grid performance. It is well known, for example, that LFA gives the exact two-grid convergence factor for problems with periodic boundary conditions.³⁸ The calculation of ρ is much cheaper, however, than direct calculation of $\rho(E_h)$ from (5). More importantly, since ρ is a function of the parameters, \mathbf{p} , arising from the relaxation scheme (or the coarse-grid correction), we can optimise ρ to achieve an optimally efficient algorithm. In our setting, such parameters appear in the diagonal scaling matrices D_i mentioned in Section 2.2.1. One of our goals in this paper is to use LFA to optimise the two-grid convergence factor of multigrid when using such relaxation schemes.

Next, we provide details on LFA for additive Vanka relaxation for the Stokes equations. Considering practical use, we first examine the stable $P_2 - P_1$ discretization, as is easily generated using general-purpose FEM tools on simplicial meshes, such as Firedrake²⁹ and FEniCS.^{43,44} We will also show LFA predictions for additive Vanka relaxation for the $Q_2 - Q_1$ discretization. The details of the symbols for the $Q_2 - Q_1$ discretization of the Stokes equations are presented in the work of He and MacLachlan¹⁸, so we only present details of these symbols for the $P_2 - P_1$ case herein.

3.3 | LFA for $P_2 - P_1$

In what follows, we consider the discretized Stokes equations, which read

$$K_h = \begin{pmatrix} -\Delta_h & 0 & (\partial_x)_h \\ 0 & -\Delta_h & (\partial_y)_h \\ -(\partial_x)_h & -(\partial_y)_h & 0 \end{pmatrix} := \begin{pmatrix} K_h^{1,1} & 0 & K_h^{1,3} \\ 0 & K_h^{2,2} & K_h^{2,3} \\ K_h^{3,1} & K_h^{3,2} & 0 \end{pmatrix}. \quad (11)$$

For the $P_2 - P_1$ discretization, the degrees of freedom for velocity are located on $\mathbf{G}_h = \bigcup_{j=1}^4 \mathbf{G}_h^j$, containing four types of meshpoints as shown at the left of Figure 1. The Laplace operator in (11) is defined by its weak form restricted to the finite-element basis functions. Here, we use the standard nodal basis and, consequently, can write this in stencil form, extending (8), with \mathbf{V} taken to be a finite index set of values, $\mathbf{V} = V_N \cup V_X \cup V_Y \cup V_C$ with $V_N \subset \mathbb{Z}^2$, $V_X \subset \{(z_x + \frac{1}{2}, z_y) | (z_x, z_y) \in \mathbb{Z}^2\}$, $V_Y \subset \{(z_x, z_y + \frac{1}{2}) | (z_x, z_y) \in \mathbb{Z}^2\}$, and $V_C \subset \{(z_x + \frac{1}{2}, z_y + \frac{1}{2}) | (z_x, z_y) \in \mathbb{Z}^2\}$. With this, the (scalar) discrete Laplace operator is naturally treated as a block operator, and the Fourier representation of each block can be calculated based on Definition 1, with the Fourier bases adapted to account for the staggering of the mesh points. Thus, the symbols of $K_h^{1,1}$ and $K_h^{2,2}$ are 4×4 matrices. Similarly to the Laplace operator, both terms in the gradient, $(\partial_x)_h$ and $(\partial_y)_h$, can be treated as (4×1) -block operators. Then, the symbols of $K_h^{1,3}$ and $K_h^{2,3}$ are 4×1 matrices, calculated based on Definition 1 adapted for the mesh staggering. The symbols of $K_h^{3,1}$ and $K_h^{3,2}$ are the conjugate transposes of those of $K_h^{1,3}$ and $K_h^{2,3}$, respectively. Accordingly, \tilde{K}_h is a 9×9 matrix for the $P_2 - P_1$ discretization.

We denote the symbols of the finite-element discretizations of the Stokes equations as

$$\tilde{K}_h(\theta_1, \theta_2) = \begin{pmatrix} \tilde{A}(\theta_1, \theta_2) & 0 & \tilde{B}_x^T(\theta_1, \theta_2) \\ 0 & \tilde{A}(\theta_1, \theta_2) & \tilde{B}_y^T(\theta_1, \theta_2) \\ \tilde{B}_x(\theta_1, \theta_2) & \tilde{B}_y(\theta_1, \theta_2) & 0 \end{pmatrix}.$$

Next, we discuss the stencils and symbols for the operators in (11). For the Laplace operator, the stencil can be split into four types which correspond to the N -, X -, Y -, and C -type points, shown in Figure 2. For the Y -type, the stencil is a 90° rotation of that of X -type, so we do not include it.

Rewriting the stencils shown in Figure 2, we can write the four stencils of $K_h^{1,1}$ as follows,

$$A_N = \frac{1}{3} \begin{bmatrix} 1 \\ -4 \\ 1 \ -4 \ 12 \ -4 \ 1 \\ -4 \\ 1 \end{bmatrix}, \quad A_X = A_Y = A_C = \frac{1}{3} \begin{bmatrix} -4 \\ -4 \ 16 \ -4 \\ -4 \end{bmatrix}.$$

Note that each stencil connects multiple types of meshpoints, so we further split each stencil into four substencils based on the type of DoFs. Taking A_N as an example, we see it connects three of the four types of meshpoints. Thus, A_N can be written

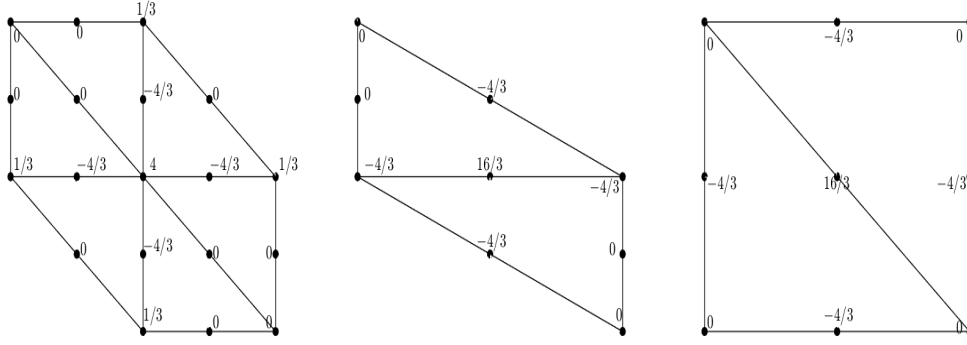


FIGURE 2 Stencils for the P_2 finite-element discretization of the Laplace operator on a left triangular grid. Left: connections from DoF at a mesh node. Middle: connections from a horizontal edge. Right: connections from a diagonal mesh edge.

as $A_N = (A_{N,N} \ A_{N,X} \ A_{N,Y} \ A_{N,C})$, where

$$A_{N,N} = \frac{1}{3} \begin{bmatrix} 1 & & & \\ 1 & 12 & 1 & \\ & & 1 & \\ & & & 1 \end{bmatrix}, \quad A_{N,X} = \frac{1}{3} [-4 \quad -4], \quad A_{N,Y} = \frac{1}{3} \begin{bmatrix} -4 \\ -4 \end{bmatrix}, \quad A_{N,C} = 0.$$

By standard calculation based on Definition 1, we have

$$\tilde{A}_{N,N} = 4 + \frac{2}{3} (\cos \theta_1 + \cos \theta_2), \quad \tilde{A}_{N,X} = -\frac{8}{3} \cos \frac{\theta_1}{2}, \quad \tilde{A}_{N,Y} = -\frac{8}{3} \cos \frac{\theta_2}{2}, \quad \tilde{A}_{N,C} = 0.$$

Similarly, $\tilde{A}_X, \tilde{A}_Y, \tilde{A}_C$ can be treated in this way. Thus, the symbol of $K_h^{1,1}$ and $K_h^{2,2}$ can be written as

$$\tilde{A}(\theta_1, \theta_2) = \begin{pmatrix} \tilde{A}_N \\ \tilde{A}_X \\ \tilde{A}_Y \\ \tilde{A}_C \end{pmatrix} = \begin{pmatrix} \tilde{A}_{N,N} & \tilde{A}_{N,X} & \tilde{A}_{N,Y} & \tilde{A}_{N,C} \\ \tilde{A}_{X,N} & \tilde{A}_{X,X} & \tilde{A}_{X,Y} & \tilde{A}_{X,C} \\ \tilde{A}_{Y,N} & \tilde{A}_{Y,X} & \tilde{A}_{Y,Y} & \tilde{A}_{Y,C} \\ \tilde{A}_{C,N} & \tilde{A}_{C,X} & \tilde{A}_{C,Y} & \tilde{A}_{C,C} \end{pmatrix},$$

with $\tilde{A}(\theta_1, \theta_2)^T = \tilde{A}(\theta_1, \theta_2)$.

From Definition 1 and the stencils in Figure 2, we have the following symbols,

$$\begin{aligned} \tilde{A}_{X,X} &= \frac{16}{3}, \quad \tilde{A}_{X,Y} = 0, \quad \tilde{A}_{X,C} = -\frac{8}{3} \cos \frac{\theta_2}{2}, \\ \tilde{A}_{Y,Y} &= \frac{16}{3}, \quad \tilde{A}_{Y,C} = -\frac{8}{3} \cos \frac{\theta_1}{2}, \quad \tilde{A}_{C,C} = \frac{16}{3}. \end{aligned}$$

Similarly to the stencil of the Laplacian operator, the stencils of $(\partial_x)_h$ and $(\partial_y)_h$ can be split into four types of substencil, respectively. Figure 3 shows the stencils of the gradient, that is, the pressure-to-velocity unknowns (N -, X -, Y - and C -type) connections, for the pressure unknown located at the middle of the hexagon.

Thus, the stencil of $(\partial_x)_h$ shown in Figure 3 can be written as $B_x^T = [B_{x,N}; B_{x,X}; B_{x,Y}; B_{x,C}]$. However, here, we calculate the stencils of $-(\partial_x)_h$ and its symbols given by

$$\begin{aligned} B_{x,N} &= 0, \quad \tilde{B}_{x,N}(\theta_1, \theta_2) = 0, \\ B_{x,X} &= \frac{h}{3} [-1 \quad 1], \quad \tilde{B}_{x,X}(\theta_1, \theta_2) = \frac{2ih}{3} \sin \frac{\theta_1}{2}, \\ B_{x,Y} &= \frac{h}{6} \begin{bmatrix} -1 & 1 & 0 \\ 0 & -1 & 1 \end{bmatrix}, \quad \tilde{B}_{x,Y}(\theta_1, \theta_2) = \frac{ih}{3} \left(\sin \frac{\theta_2}{2} + \sin \theta_1 \cos \frac{\theta_2}{2} - \cos \theta_1 \sin \frac{\theta_2}{2} \right), \\ B_{x,C} &= \frac{h}{6} \begin{bmatrix} -1 & 1 \\ -1 & 1 \end{bmatrix}, \quad \tilde{B}_{x,C}(\theta_1, \theta_2) = \frac{2ih}{3} \sin \frac{\theta_1}{2} \cos \frac{\theta_2}{2}, \end{aligned}$$

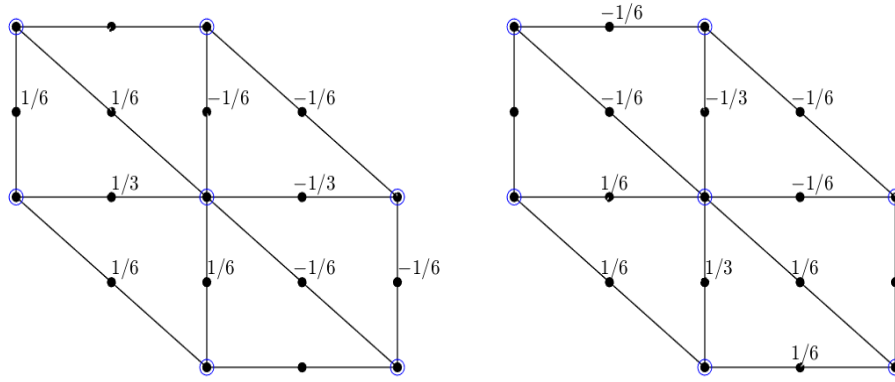


FIGURE 3 Stencils for the $P_2 - P_1$ finite-element discretization of the derivative operators on a left triangular grid. Left: $(\partial_x)_h$ stencil with a scaling h . Right: $(\partial_y)_h$ stencil with a scaling h . The (blue) circles at the center are the locations of pressure unknowns and the marked points without a given weight have value 0.

respectively.

Similarly to $\tilde{B}_x(\theta_1, \theta_2)^T$, the symbol of the stencil of $(\partial_y)_h$ can be written as

$$\tilde{B}_y(\theta_1, \theta_2)^T = [\tilde{B}_{x,N}(\theta_2, \theta_1); \tilde{B}_{x,Y}(\theta_2, \theta_1); \tilde{B}_{x,X}(\theta_2, \theta_1); \tilde{B}_{x,C}(\theta_2, \theta_1)].$$

Remark 3. Rodrigo et al.⁴⁵ presented a framework for LFA for edge-based discretizations on triangular grids. They consider an expression for the Fourier transform in a non-orthogonal coordinate system in space and frequency variables to adapt to arbitrary structured triangular meshes. This idea can be applied to the discretization considered here. However, for the triangle mesh considered here, it is not necessary to use non-orthogonal coordinates. In the framework of LFA provided here, we use a different Fourier basis to be consistent with the different types of stencil located on different types of grid-points, which simplifies the calculation.

3.4 | LFA representation of Grid-transfer operators

Here, we use the standard finite-element interpolation operators and their transposes for restriction. In the following, we discuss the stencils and symbols of these restriction and interpolation operators.

To derive symbols for the grid-transfer operators, we first consider an arbitrary restriction operator characterized by a constant coefficient stencil $R_h \hat{=} [r_\kappa]$. Then, an infinite grid function $w_h : \mathbf{G}_h^1 \rightarrow \mathbb{R}$ (or \mathbb{C}) is transferred to the coarse grid, \mathbf{G}_{2h}^1 , in the following way

$$(R_h w_h)(\mathbf{x}) = \sum_{\kappa \in V} r_\kappa w_h(\mathbf{x} + \kappa h) \quad (\mathbf{x} \in \mathbf{G}_{2h}^1).$$

Taking w_h to be the Fourier mode, $\varphi(\theta^\alpha, \mathbf{x}) = e^{i\theta^\alpha \cdot \mathbf{x}/h}$, we have

$$(R_h \varphi(\theta^\alpha, \cdot))(\mathbf{x}) = \tilde{R}_h(\theta^\alpha) \varphi_{2h}(2\theta^{(0,0)}, \mathbf{x}) \quad (\mathbf{x} \in \mathbf{G}_{2h}^1), \quad (12)$$

with $\tilde{R}_h(\theta^\alpha) = \sum_{\kappa \in V} r_\kappa e^{i\kappa \cdot \theta^\alpha}$, which is called the symbol of R_h . However, since we consider discretizations on staggered meshes, where different “types” of variables interact in the interpolation and restriction operators, the symbol definition for the restriction operator acting on \mathbf{G}_{2h}^j , where $j = 2, 3, 4$, must be modified.

Similarly to the stencils of K_h , the restriction operator for the components of velocity can also be decomposed based on the partitioning of the DoFs associated with the N -, X -, Y -, and C -type meshpoints. Each of these restriction operators connects between all four types of meshpoints, and we partition each restriction operator into four blocks based on the DoFs. For $\mathbf{x} \in \mathbf{G}_{2h}^j$, where $j = 1, \dots, 4$, by standard calculation,⁴² (12) becomes

$$(R_h \varphi(\theta^\alpha, \cdot))(\mathbf{x}) = \sum_{\kappa \in V} r_\kappa e^{i\kappa \cdot \theta^\alpha} e^{i\alpha \cdot \pi \mathbf{x}/h} \varphi_{2h}(2\theta^{(0,0)}, \mathbf{x}).$$

While $e^{i\alpha \cdot \pi x/h}$ appears in the above formulation, it serves only to indicate which type of DoF R_h is acting on, since

$$e^{i\alpha \cdot \pi x/h} = \begin{cases} 1, & \text{for } \mathbf{x} \in \mathbf{G}_{2h}^1, \\ (-1)^{\alpha_1}, & \text{for } \mathbf{x} \in \mathbf{G}_{2h}^2, \\ (-1)^{\alpha_2}, & \text{for } \mathbf{x} \in \mathbf{G}_{2h}^3, \\ (-1)^{\alpha_1}(-1)^{\alpha_2}, & \text{for } \mathbf{x} \in \mathbf{G}_{2h}^4. \end{cases}$$

Thus, it is natural to give the following general definition of a restriction symbol on a staggered mesh.

Definition 4. We call $\tilde{R}(\theta^\alpha) = \sum_{\kappa \in \mathcal{V}} r_\kappa e^{i\kappa \cdot \theta^\alpha} e^{i\alpha \cdot \pi x/h}$ the restriction symbol of R_h .

We emphasize that we must first split the restriction operator into the different types of DoFs that it restricts from and to before we can apply Definition 4.

We first consider restriction to the N -type DoFs of a P_2 function, which can be split into four blocks,

$$R_{v,N} = [R_{N,N} \ R_{N,X} \ R_{N,Y} \ R_{N,C}].$$

The N -to- N connection is

$$R_{N,N} = [1 \star],$$

where the \star denotes the position (on the coarse grid) at which the discrete operator is applied. From Definition 4, $\tilde{R}_{N,N} = 1$. The X -to- N connections yield the stencil

$$R_{N,X} = \frac{1}{8} \begin{bmatrix} -1 & & -1 & & \\ -1 & 3 & \star & 3 & -1 \\ & & -1 & & -1 \end{bmatrix}.$$

By standard calculation, we have

$$\tilde{R}_{N,X} = \frac{1}{4} \left(3 \cos \frac{\theta_1}{2} - \cos \frac{3\theta_1}{2} - \cos \frac{\theta_1}{2} \cos \theta_2 + \sin \frac{\theta_1}{2} \sin \theta_2 - \cos \frac{3\theta_1}{2} \cos \theta_2 - \sin \frac{3\theta_1}{2} \sin \theta_2 \right).$$

Similarly, the Y -to- N connection has the stencil

$$R_{N,Y} = \frac{1}{8} \begin{bmatrix} -1 & -1 & & & \\ & 3 & -1 & & \\ & & \star & & \\ -1 & 3 & & & \\ & & -1 & -1 & \end{bmatrix},$$

with its symbol

$$\tilde{R}_{N,Y} = \frac{1}{4} \left(3 \cos \frac{\theta_2}{2} - \cos \frac{3\theta_2}{2} - \cos \theta_1 \cos \frac{\theta_2}{2} + \sin \theta_1 \sin \frac{\theta_2}{2} - \cos \theta_1 \cos \frac{3\theta_2}{2} - \sin \theta_1 \sin \frac{3\theta_2}{2} \right).$$

The C -to- N connection has the stencil

$$R_{N,C} = \frac{1}{8} \begin{bmatrix} -1 & -1 & & & \\ -1 & 3 & & & \\ & & & \star & \\ & & & & 3 & -1 \\ & & & & -1 & -1 \end{bmatrix},$$

with its symbol

$$\begin{aligned} \tilde{R}_{N,C} = \frac{1}{8} & \left(3 \cos \frac{\theta_1}{2} \cos \frac{\theta_2}{2} - 3 \sin \frac{\theta_1}{2} \sin \frac{\theta_2}{2} - \cos \frac{3\theta_1}{2} \cos \frac{3\theta_2}{2} - \sin \frac{3\theta_1}{2} \sin \frac{3\theta_2}{2} \right. \\ & \left. - \cos \frac{3\theta_1}{2} \cos \frac{\theta_2}{2} - \sin \frac{3\theta_1}{2} \sin \frac{\theta_2}{2} - \cos \frac{\theta_1}{2} \cos \frac{3\theta_2}{2} - \sin \frac{\theta_1}{2} \sin \frac{3\theta_2}{2} \right). \end{aligned}$$

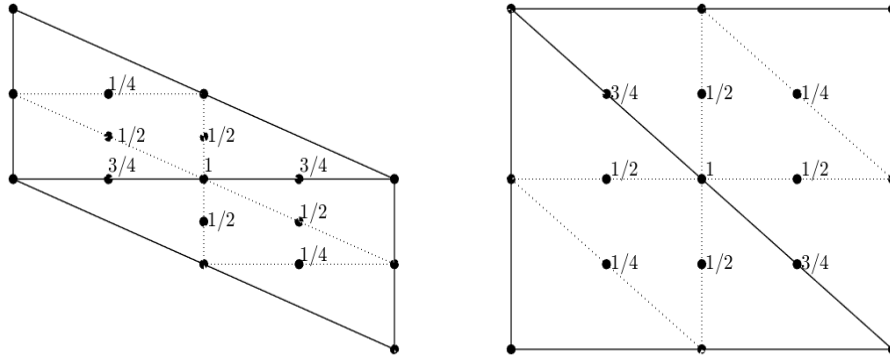


FIGURE 4 Restriction stencils for the P_2 finite-element discretization of the Laplace operator on a left triangular grid. The solid triangles denote elements from the coarse-grid and the dashed triangles are those of the fine-grid. Left: $R_{v,X}$. Right: $R_{v,C}$.

TABLE 1 Symbols of $R_{v,X}$, $R_{v,Y}$ and $R_{v,C}$

*	$R_{*,N}$	$R_{*,X}$	$R_{*,Y}$	$R_{*,C}$
X	1	$\frac{3}{2} \cos \theta_1 + \frac{1}{2} (\cos \frac{\theta_1}{2} \cos \theta_2 + \sin \frac{\theta_1}{2} \sin \theta_2)$	$\cos \frac{\theta_2}{2}$	$\cos \frac{\theta_1}{2} \cos \frac{\theta_2}{2} + \sin \frac{\theta_1}{2} \sin \frac{\theta_2}{2}$
Y	1	$\cos \frac{\theta_1}{2}$	$\frac{3}{2} \cos \theta_2 + \frac{1}{2} (\cos \theta_1 \cos \frac{\theta_2}{2} + \sin \theta_1 \sin \frac{\theta_2}{2})$	$\cos \frac{\theta_1}{2} \cos \frac{\theta_2}{2} + \sin \frac{\theta_1}{2} \sin \frac{\theta_2}{2}$
C	1	$\cos \frac{\theta_1}{2}$	$\cos \frac{\theta_2}{2}$	$2 \cos \frac{\theta_1}{2} \cos \frac{\theta_2}{2} + \sin \frac{\theta_1}{2} \sin \frac{\theta_2}{2}$

The weights for the X -type and C -type restrictions for P_2 are shown in Figure 4. For the Y -type DoFs, the restriction stencil is a 90° rotation of that of X -type, so we do not include it. We use the same decomposition for $R_{v,X}$, $R_{v,Y}$ and $R_{v,C}$, and their symbols are listed in Table 1.

Following Definition 4 to account for staggering, we can write

$$\tilde{R}_v(\theta^{00}) = \begin{pmatrix} \tilde{R}_{v,N}(\theta^{00}) \\ \tilde{R}_{v,X}(\theta^{00}) \\ \tilde{R}_{v,Y}(\theta^{00}) \\ \tilde{R}_{v,C}(\theta^{00}) \end{pmatrix}, \quad \tilde{R}_v(\theta^{10}) = \begin{pmatrix} \tilde{R}_{v,N}(\theta^{10}) \\ -\tilde{R}_{v,X}(\theta^{10}) \\ \tilde{R}_{v,Y}(\theta^{10}) \\ -\tilde{R}_{v,C}(\theta^{10}) \end{pmatrix}, \quad \tilde{R}_v(\theta^{01}) = \begin{pmatrix} \tilde{R}_{v,N}(\theta^{01}) \\ \tilde{R}_{v,X}(\theta^{01}) \\ -\tilde{R}_{v,Y}(\theta^{01}) \\ -\tilde{R}_{v,C}(\theta^{01}) \end{pmatrix}, \quad \tilde{R}_v(\theta^{11}) = \begin{pmatrix} \tilde{R}_{v,N}(\theta^{11}) \\ -\tilde{R}_{v,X}(\theta^{11}) \\ -\tilde{R}_{v,Y}(\theta^{11}) \\ \tilde{R}_{v,C}(\theta^{11}) \end{pmatrix}.$$

Interpolation, P_v , is taken to be the transpose of R_v , with symbol $\tilde{P}_v(\theta^\alpha) = \frac{1}{4} \tilde{R}_v^T(\theta^\alpha)$.

All of the pressure DoFs are located on \mathbf{G}_h^1 . Thus, the restriction operator for pressure acts only on one type of grid point, the nodes of the mesh. The stencil of the restriction operator for pressure is given by

$$R_p = \frac{1}{2} \begin{bmatrix} 1 & 1 \\ 1 & 2\star & 1 \\ & 1 & 1 \end{bmatrix},$$

with its symbol

$$\tilde{R}_p(\theta_1, \theta_2) = 1 + \cos \theta_1 + \cos \theta_2 + \cos \theta_1 \cos \theta_2 + \sin \theta_1 \sin \theta_2.$$

The interpolation, P_p , for pressure is taken to be the transpose of R_p , with symbol $\tilde{P}_p(\theta_1, \theta_2) = \frac{1}{4} \tilde{R}_p(\theta_1, \theta_2)^T$.

Finally, the restriction operator for the Stokes system can be written as

$$R_h = \begin{bmatrix} R_v & 0 & 0 \\ 0 & R_v & 0 \\ 0 & 0 & R_p \end{bmatrix},$$

with its symbol (over all four harmonics) being a 9×36 matrix. For the interpolation operator, P_h , we consider the transpose of R_h , and the symbols satisfy

$$\tilde{P}_h(\boldsymbol{\theta}) = \frac{1}{4} \tilde{R}_h^T(\boldsymbol{\theta}).$$

For the coarse-grid operator, K_H , we consider rediscrretization, which is equivalent to Galerkin coarsening.

3.5 | LFA for additive Vanka relaxation

When applying LFA to overlapping multiplicative Vanka relaxation, multiple Fourier representations are required for each variable in a given patch to account for the intermediate ‘‘stages’’ in the relaxation²⁴. This is not needed in the additive case considered here. Unlike classical relaxation, additive Vanka relaxation is a block relaxation scheme. Since the variables on each block are updated at the same time, based on the same block system, we can apply LFA ideas, but must modify the standard LFA to include a block Fourier basis to represent all the information in each block. By Fourier transformation the operator M_h^{-1} , defined on an infinite mesh, can be block diagonalized (by appropriately ordering the unknowns).

Recall $M_h^{-1} = \sum_{i=1}^N V_i^T D_i K_i^{-1} V_i$. Under the Fourier ansatz, D_i , V_i and K_i have the same representation for all i . Note that since D_i is a diagonal scaling matrix, its Fourier representation is itself. Similarly, V_i is a projector, and its symbol is itself. Note that the representation of K_i^{-1} is equal to the inverse of the representation of K_i . Thus, we only need to consider the representation of K_i . Assume that the set of grid points corresponding to the DoFs of K_i is $\Xi_i = \{\mathbf{x}_1^{(i)}, \dots, \mathbf{x}_m^{(i)}\} \subseteq \mathbf{G}_h$ and assume the ordering of the DoFs in K_i is consistent with the ordering of points in Ξ_i . Note that, due to the overlap between subdomains in the Schwarz relaxation, Ξ_i might contain multiple points with the same Fourier representation in the symbol of (11), but we treat them separately in the representation of K_i , since these points correspond to different unknowns in \mathfrak{S}_i . Let

$$\varpi = \text{span} \left\{ \psi_j(\boldsymbol{\theta}) = e^{i\boldsymbol{\theta} \cdot \mathbf{x}_j^{(i)}/h} \cdot \chi_j, j = 1, \dots, m \right\},$$

where χ_j is an $m \times 1$ vector with only one nonzero element with value 1 located in the j -th position.

Let us consider the action of K_i on this Fourier basis on Ξ_i , defining the symbol, \tilde{K}_i , so that

$$K_i \psi(\boldsymbol{\theta}) = \tilde{K}_i \psi(\boldsymbol{\theta}), \forall \psi \in \varpi. \quad (13)$$

Let Φ be an $m \times m$ diagonal matrix with diagonal elements, $e^{i\boldsymbol{\theta} \cdot \mathbf{x}_j^{(i)}/h}$ for $j = 1, 2, \dots, m$, and $\boldsymbol{\alpha} = (\alpha_1, \alpha_2, \dots, \alpha_m)^T$ be an arbitrary vector. Then, (13) is equivalent to

$$K_i \sum_{j=1}^m \alpha_j \psi_j = K_i \Phi \boldsymbol{\alpha} = \Phi \tilde{K}_i \boldsymbol{\alpha}. \quad (14)$$

Thus, from (14), the Fourier representation of K_i is

$$\tilde{K}_i = \Phi^{-1} K_i \Phi = \Phi^T K_i \Phi. \quad (15)$$

Note that, under the Fourier ansatz, all of these matrices are independent of i except for our construction of Φ . However, due to the special structure of Φ , we can use relative values of nodal position to replace the matrix Φ in (15) by a simple matrix (called the relative Fourier matrix), scaled by $e^{i\boldsymbol{\theta} \cdot \mathbf{x}_s^{(i)}/h}$, for some $\mathbf{x}_s^{(i)} \in \Xi_i$. This is equivalent to considering the Fourier basis acting on a local offset, $\mathbf{x}_j^{(i)} := \mathbf{x}_j^{(i)} - \mathbf{x}_s^{(i)}$ for some fixed point $\mathbf{x}_s^{(i)}$ in the patch, usually the pressure node. As this scaling simplifies the calculation, we will use the relative Fourier matrix in the rest of the paper.

3.6 | LFA for additive Vanka relaxation for the Stokes equations

Now, we consider LFA for two types of Vanka relaxation schemes that differ only in the choice of the relaxation blocks. First, for each pressure DoF, we consider patches containing all velocity DoFs included in a hexagon centred at the node associated with the pressure, see left of Figure 5 for the $P_2 - P_1$ discretization. This patch is the smallest one that contains all velocity DoFs with connections to this pressure DoF in the symbolic nonzero pattern of the matrix. For this reason, we refer to this patch construction as Vanka-inclusive (VKI). The number of DoFs in this patch for $P_2 - P_1$ is 39. To be specific, there are 7 N -type points, 4 points for X -, Y - and C -type, respectively, for each of the two components of the velocity, and 1 N -type point for the central pressure, see Table 2. Since the patches and submatrices K_i are the same, it is natural to consider D_i to be the same for all i . For D_i in (6), a simple idea is to take D_i to be the identity, which we refer to as using *no weights*. Another choice for D_i is to take d_{m_i} in D_i to be the reciprocal of the number of patches that each type of DoF appears in. We refer to this as using *geometric weights* (or *natural weights*), and will denote this by VKIW in the results to follow. To be specific, the weights for the

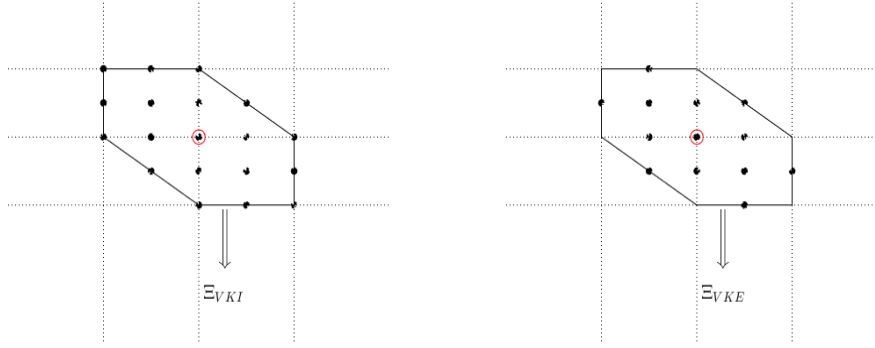


FIGURE 5 Left: Vanka-inclusive patch for the $P_2 - P_1$ discretization. Right: Vanka-exclusive patch for the $P_2 - P_1$ discretization.

TABLE 2 The number (#) of different type of DoFs for Vanka-inclusive and Vanka-exclusive patches for the $P_2 - P_1$ and $Q_2 - Q_1$ discretizations.

patch \ #	$P_2 - P_1$		$Q_2 - Q_1$	
	Ξ_{VKI}	Ξ_{VKE}	Ξ_{VKI}	Ξ_{VKE}
each component of velocity				
N	7	1	9	1
X	4	4	6	6
Y	4	4	6	6
C	4	4	4	4
pressure				
N	1	1	1	1
Total	39	27	51	35

velocity DoFs are $1/7$, $1/4$, $1/4$, and $1/4$ for the N -, X -, Y - and C - type points, respectively. For pressure, the natural weight is 1. Thus, D_i is a 39×39 matrix given by

$$D_i = \begin{pmatrix} D_v & 0 & 0 \\ 0 & D_v & 0 \\ 0 & 0 & D_p \end{pmatrix}, \text{ with } D_v = \begin{pmatrix} D_N & 0 & 0 & 0 \\ 0 & D_X & 0 & 0 \\ 0 & 0 & D_Y & 0 \\ 0 & 0 & 0 & D_C \end{pmatrix}, D_p = 1,$$

where $D_N = \frac{1}{7}I_{7 \times 7}$ and $D_X = D_Y = D_C = \frac{1}{4}I_{4 \times 4}$. Since \tilde{K}_h is a 9×9 matrix, the symbol of V_i is a 39×9 projection matrix. Finally, \tilde{K}_i is a 39×39 matrix, as is D_i .

Now, we give more details about how to calculate the relative Fourier matrix, Φ . For $P_2 - P_1$, with patches Ξ_{VKI} as shown at the left of Figure 5, we take $x_s^{(i)}$ be the node located directly below the central pressure DoF. We use lexicographical order to order the remaining points in Ξ_{VKI} for each type of point (N -, X -, Y -, and C - ordering), that is, from left to right and bottom to top. Then,

$$\Phi(\theta_1, \theta_2) = \begin{pmatrix} \Phi_v & 0 & 0 \\ 0 & \Phi_v & 0 \\ 0 & 0 & \Phi_p \end{pmatrix}, \quad (16)$$

where

$$\begin{aligned}
\Phi_n &= [1, e^{i\theta_1}, e^{-i\theta_1+i\theta_2}, e^{i\theta_2}, e^{i\theta_1+i\theta_2}, e^{-i\theta_1+i2\theta_2}, e^{i2\theta_2}], \\
\Phi_x &= [e^{i/2\theta_1}, e^{-i/2\theta_1+i\theta_2}, e^{i/2\theta_1+i\theta_2}, e^{-i/2\theta_1+i2\theta_2}], \\
\Phi_y &= [e^{i/2\theta_2}, e^{i\theta_1+i/2\theta_2}, e^{-i\theta_1+i3/2\theta_2}, e^{i3/2\theta_2}], \\
\Phi_c &= [e^{-i/2\theta_1+i/2\theta_2}, e^{i/2\theta_1+i/2\theta_2}, e^{-i/2\theta_1+i3/2\theta_2}, e^{i/2\theta_1+i3/2\theta_2}], \\
\Phi_0 &= [\Phi_n, \Phi_x, \Phi_y, \Phi_c], \\
\Phi_v &= \text{diag}(\Phi_0), \\
\Phi_p &= e^{i\theta_2}.
\end{aligned}$$

Remark 4. Note that matrix Φ in (16) is only a function of frequency, $\theta = (\theta_1, \theta_2)$, and is independent of the meshsize, h , and the index i .

For V_i , mapping the global vector to the vector on the patch, we only need to account for the duplication that arises from the representation of the global Fourier basis of dimension 9 to the local block representation. Here, the order follows N -type, X -type, Y -type, then C -type, and velocity is first, then followed by the pressure. The structure is

$$\tilde{V}_i = \begin{pmatrix} V_v & 0 & 0 \\ 0 & V_x & 0 \\ 0 & 0 & V_p \end{pmatrix},$$

where $V_p = 1$ and V_v is a 19×4 matrix defined as follows

$$V_v = \begin{pmatrix} I_N & 0 & 0 & 0 \\ 0 & I_X & 0 & 0 \\ 0 & 0 & I_Y & 0 \\ 0 & 0 & 0 & I_C \end{pmatrix} \quad (17)$$

where I_N is the 7×1 vector of all ones, and $I_X = I_Y = I_C$ are the 4×1 vector of all ones.

Considering the stencils in Figure 3, we note that of the adjacent nodal velocity DoFs, only the central one appears in the gradient operator. This motivates construction of a second patch that contains all of the DoFs in VKI except for the N -type velocity DoFs at the edges of the VKI patch, see the right of Figure 5. We refer to this as Vanka-exclusive (VKE) when used with no weights ($D_i = I$). Table 2 presents the number of the four types of DoFs for VKE, which contains $39 - 2 \cdot 6 = 27$ DoFs in total. Another choice for D_i is to use the natural weights, which we refer to as Vanka-exclusive with natural weights (VKEW). Here, the weights are $1, 1/4, 1/4, 1/4$ for N -, X -, Y - and C - type velocity DoFs, respectively, and 1 for pressure. Similarly to VKI, we can calculate the matrix Φ whose size is 27×27 following (16), replacing Φ_n by $\Phi_n = e^{i\theta_2}$. For \tilde{V}_i , there is only 1 N -type point for velocity, so we only need to modify I_N to be the scalar 1 in (17), then we obtain \tilde{V}_i , which is a 27×9 matrix. In each of these cases, the overall symbol for relaxation is a 9×9 matrix. Since we consider four harmonics, following subsection 3.2, \tilde{E}_h is a 36×36 matrix. In the rest of this paper, we omit the subscript h unless it is necessary to avoid confusion.

For the $Q_2 - Q_1$ discretization of the Stokes equations, the patches of Vanka-inclusive and Vanka-exclusive are a little different than the structure with the $P_2 - P_1$ discretizations. Figure 6 shows the Vanka-inclusive and Vanka-exclusive patches for the $Q_2 - Q_1$ discretization, and Table 2 lists the details. For VKI, the numbers of unknowns for the velocity are 9, 6, 6, 4 for N -, X -, Y -, and C -types, respectively. In total, there are $2(9 + 6 + 6 + 4) + 1 = 51$ DoFs in one patch. To construct V_v , we only need to change I_N in (17) to be the 9×1 vector of all ones, and $I_X = I_Y$ to be the 6×1 vectors of all ones. As in the $P_2 - P_1$ case, the $Q_2 - Q_1$ gradient operator on a uniform mesh uses only the central nodal velocity DoF. Thus, the second patch contains all of the DoFs in VKI except for the N -type points at the edges of the block, giving $51 - 2 \cdot 8 = 35$ DoFs. To obtain the representation of V_i using VKE for $Q_2 - Q_1$ from the construction of V_v for VKI with the $Q_2 - Q_1$ discretization, we only need to change I_N to a scalar 1.

We again use the relative Fourier matrix, Φ , to transform, the block matrix, K_i . We set $\mathbf{x}_s^{(i)}$ to be the lower-left corner at the block, giving,

$$\Phi(\theta_1, \theta_2) = \begin{pmatrix} \Phi_{Q_v} & 0 & 0 \\ 0 & \Phi_{Q_v} & 0 \\ 0 & 0 & \Phi_{Q_p} \end{pmatrix}, \quad (18)$$

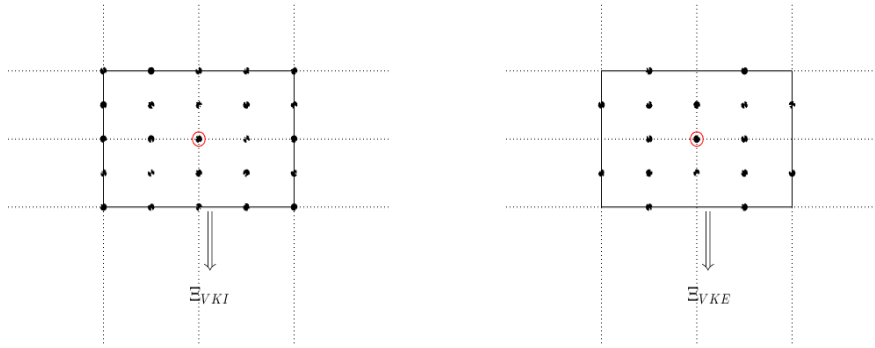


FIGURE 6 Left: Vanka-inclusive patch for the $Q_2 - Q_1$ discretization. Right: Vanka-exclusive patch for the $Q_2 - Q_1$ discretization.

where

$$\begin{aligned}
 \Phi_{Q_n} &= [1, e^{i\theta_1}, e^{i2\theta_1}, e^{i\theta_2}, e^{i\theta_1+i\theta_2}, e^{i2\theta_1+i\theta_2}, e^{i2\theta_2}, e^{i\theta_1+i2\theta_2}, e^{i2\theta_1+i2\theta_2}], \\
 \Phi_{Q_x} &= [e^{i/2\theta_1}, e^{i3/2\theta_1}, e^{i/2\theta_1+i\theta_2}, e^{i3/2\theta_1+i\theta_2}, e^{i/2\theta_1+i2\theta_2}, e^{i3/2\theta_1+i2\theta_2}], \\
 \Phi_{Q_y} &= [e^{i/2\theta_2}, e^{i\theta_1+i/2\theta_2}, e^{i2\theta_1+i/2\theta_2}, e^{i3/2\theta_2}, e^{i\theta_1+i3/2\theta_2}, e^{i2\theta_1+i3/2\theta_2}], \\
 \Phi_{Q_c} &= [e^{i/2\theta_1+i/2\theta_2}, e^{i3/2\theta_1+i/2\theta_2}, e^{i/2\theta_1+i3/2\theta_2}, e^{i3/2\theta_1+i3/2\theta_2}], \\
 \Phi_{Q_0} &= [\Phi_{Q_n}, \Phi_{Q_x}, \Phi_{Q_y}, \Phi_{Q_c}], \\
 \Phi_{Q_v} &= \text{diag}(\Phi_{Q_0}), \\
 \Phi_{Q_p} &= e^{i\theta_1+i\theta_2}.
 \end{aligned}$$

For VKE with $Q_2 - Q_1$, we truncate Φ_{Q_n} to the scalar $e^{i\theta_1+i\theta_2}$.

4 | PARAMETER CHOICE AND VALIDATION

As a relaxation scheme, we consider the Chebyshev iteration⁴⁰ on K_h preconditioned with overlapping additive Vanka, with the two patches discussed before. We note that this is the natural extension of weighted Jacobi to block relaxation when considering more than a single relaxation sweep per level in a two-grid cycle. The key point to tuning the Chebyshev iteration is the choice of the lower and upper bounds for the interval that determines the Chebyshev polynomials. LFA is useful here, and we employ it to find optimal bounds for different degrees of Chebyshev polynomials. Relaxation using both no weights and natural weights will be considered. As a special case, we also consider a simple preconditioned Richardson relaxation, for the cases $\nu_1 + \nu_2 = 1$ and $\nu_1 + \nu_2 = 2$, where we again use LFA to help find the optimal weights. The goal of these experiments is to use LFA to determine “best practices” in terms of how to choose patches and weights, with relaxation parameters optimized for these choices. Finally, we compare the cost and performance among these approaches.

In practice, the LFA two-grid convergence factors often exactly match the true convergence factor of multigrid applied to a problem with periodic boundary conditions.^{37, 46} For the case of Dirichlet boundary conditions, a gap between the LFA predictions and the actual performance is sometimes observed.^{10, 17, 18} In order to see the influence of boundary conditions on multigrid performance, we present data for both Dirichlet and periodic boundary conditions. Our tests are implemented using Firedrake and PETSc³¹ for both the $P_2 - P_1$ and $Q_2 - Q_1$ discretizations. The subproblems associated with K_i are solved by LU decomposition. We focus on optimizing the interval used for Chebyshev relaxation with symmetric pre- and post-relaxation.

TABLE 3 Two-grid LFA predictions for Chebyshev Vanka relaxation and two-grid performance with periodic ($\hat{\rho}$) and Dirichlet ($\hat{\rho}^D$) boundary conditions for the $P_2 - P_1$ discretization for VKI. Optimal intervals for different k with no weights. An alternating convergence pattern was observed, so the reported convergence factor is averaged over the final seven iterations before convergence (denoted *).

LFA predictions			$h = \frac{1}{20}$		$h = \frac{1}{40}$		$h = \frac{1}{80}$	
k	$[\alpha, \beta]_{\text{VKI}}$	ρ_{VKI}	$\hat{\rho}_{\text{VKI}}$	$\hat{\rho}_{\text{VKI}}^D$	$\hat{\rho}_{\text{VKI}}$	$\hat{\rho}_{\text{VKI}}^D$	$\hat{\rho}_{\text{VKI}}$	$\hat{\rho}_{\text{VKI}}^D$
1	[0.1, 8.3]	0.679	0.672	0.699	0.671	0.699	0.671	0.699
2	[0.9, 7.8]	0.295	0.296	0.585	0.296	0.585	0.296	0.585
3	[0.9, 7.9]	0.120	0.107*	0.148	0.133*	0.148	0.143*	0.148
4	[1.4, 7.2]	0.102	0.102	0.133	0.102	0.133	0.102	0.133
5	[1.3, 7.4]	0.051	0.050	0.074	0.049	0.074	0.047	0.074

4.1 | Numerical results for the $P_2 - P_1$ discretization

4.1.1 | No weights

First, we consider $D_i = I$ and the two different patches discussed above. The two-grid error iteration matrix is

$$E_k = p_k(T) \mathcal{M}^{\text{CGC}} p_k(T), \quad (19)$$

where $T = M_h^{-1} K_h$ and p_k is the Chebyshev polynomial with degree k on a given interval. Below, we take ρ to be the LFA prediction sampled at 32 equispaced points in each dimension of the Fourier domain. (When sampling the frequency space at more points, the predictions go up only slightly.) We take $\hat{\rho}$ to be the measured convergence factor per iteration defined by $\hat{\rho}_j = \frac{\|e_j\|}{\|e_{j-1}\|}$, where $e_j = b_h - K_h u_j$, measured for problem (3) with zero right-hand side and random initial guess at the iteration when the residual norm is first below 10^{-150} . Since the discretized problem is singular, we project the approximate solution after each iteration to ensure that it remains orthogonal to the null space.

In order to find the optimal intervals for the Chebyshev iteration for different k , we use a brute force search with stepsize 0.1 to optimize the intervals with LFA. The optimal interval, denoted as $[\alpha, \beta]$, and the corresponding convergence factors are given in the following tables. Tables 3 and 4 give the measured convergence for periodic and Dirichlet boundary conditions versus the LFA predictions for different k and the corresponding optimal intervals with $h = \frac{1}{20}$, $\frac{1}{40}$, and $\frac{1}{80}$. We see that the measured convergence factors are largely independent of the meshsize, h . A good match is generally seen between the LFA predictions and the measured convergence factors, with only a tiny gap between the LFA prediction and the measured convergence factor. It is reasonable that such a gap exists for the Dirichlet case, since the LFA prediction is of the expected asymptotic convergence factor for the problem with periodic boundary conditions. This might also suggest that extra work is needed to reduce this gap.¹⁰ Note that only for $k = 2$ and VKI is this gap significant. We have also tested some other intervals for this case, seeing that the gap between the LFA prediction and the measured results with Dirichlet boundary conditions is quite variable, with some parameter values coming close to the LFA prediction, but never achieving a good agreement. For VKI with $k = 3$ and periodic boundary conditions, the per iteration measured convergence factor oscillates, but the long-term average still approaches that given by LFA. For these cases, we present averaged convergence over the final seven iterations. These tables indicate that when $k = 1$, VKE is more effective than VKI; however, for $k > 1$, the opposite occurs.

Remark 5. In the numerical tests, we see that for some cases, the optimal pair of $[\alpha, \beta]$ are not unique. We break such ties arbitrarily.

In Figure 7, we show the LFA amplification factors using Chebyshev Vanka relaxation with $k = 1$ and the parameters from Tables 3 and 4 in (19) for the $P_2 - P_1$ discretization. We see that the VKE reduces the high-frequency error faster than VKI, and both reduce the low-frequency error slowly. In Figure 8, we present the spectrum of the associated two-grid error-propagation operators. The distribution of the eigenvalues is notably different: For VKI, most of the eigenvalues are real, while, for VKE, the eigenvalues are clustered around a circle in the complex plane.

TABLE 4 Two-grid LFA predictions for Chebyshev Vanka relaxation and two-grid performance with periodic ($\hat{\rho}$) and Dirichlet ($\hat{\rho}^D$) boundary conditions for the $P_2 - P_1$ discretization for VKE. Optimal intervals for different k with no weights.

LFA predictions			$h = \frac{1}{20}$		$h = \frac{1}{40}$		$h = \frac{1}{80}$	
k	$[\alpha, \beta]_{\text{VKE}}$	ρ_{VKE}	$\hat{\rho}_{\text{VKE}}$	$\hat{\rho}_{\text{VKE}}^D$	$\hat{\rho}_{\text{VKE}}$	$\hat{\rho}_{\text{VKE}}^D$	$\hat{\rho}_{\text{VKE}}$	$\hat{\rho}_{\text{VKE}}^D$
1	[0.3, 6.0]	0.475	0.476	0.571	0.491	0.571	0.475	0.571
2	[0.5, 4.7]	0.440	0.412	0.392	0.485	0.419	0.388	0.463
3	[1.2, 4.6]	0.168	0.169	0.175	0.169	0.176	0.168	0.176
4	[1.6, 4.6]	0.127	0.125	0.124	0.128	0.127	0.127	0.127
5	[2.6, 3.7]	0.112	0.111	0.108	0.111	0.111	0.112	0.111

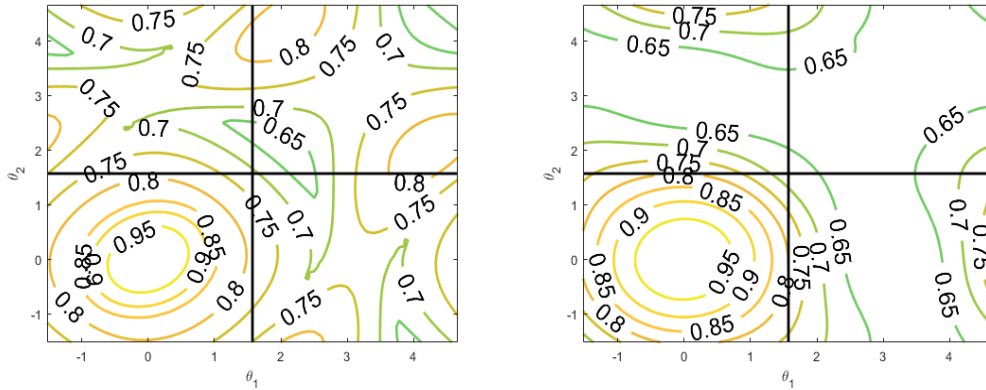


FIGURE 7 The LFA amplification factors for Vanka-relaxation with $k = 1$ for the $P_2 - P_1$ discretization. Left: VKI with $k = 1$. Right: VKE with $k = 1$.

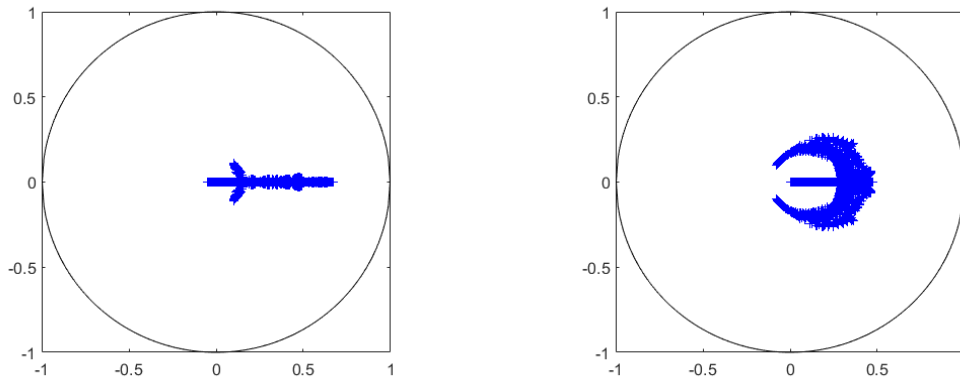


FIGURE 8 The LFA-predicted spectra of the two-grid error-propagation operators for the $P_2 - P_1$ discretization. Left: VKI with $k = 1$. Right: VKE with $k = 1$.

4.1.2 | Geometric weights

As seen in Tables 3 and 4, the measured convergence factors are largely independent of meshsize. Thus, we only consider $h = \frac{1}{40}$ in the following tests. Table 5 gives the measured convergence versus LFA predictions for relaxation with natural weights and the corresponding optimal intervals. We see a good agreement between the LFA predictions and the measured convergence factors. For the case of Dirichlet boundary conditions, the LFA predictions match the measured convergence factors very well

TABLE 5 Two-grid LFA predictions for Chebyshev Vanka relaxation and multigrid performance with periodic ($\hat{\rho}$) and Dirichlet ($\hat{\rho}^D$) boundary conditions for the $P_2 - P_1$ discretization. Optimal intervals for different k with natural weights. $h = \frac{1}{40}$.

k	$[\alpha, \beta]_{\text{VKIW}}$	ρ_{VKIW}	$\hat{\rho}_{\text{VKIW}}$	$\hat{\rho}_{\text{VKIW}}^D$	$[\alpha, \beta]_{\text{VKEW}}$	ρ_{VKEW}	$\hat{\rho}_{\text{VKEW}}$	$\hat{\rho}_{\text{VKEW}}^D$
1	[0.9, 2.9]	0.518	0.518	0.517	[1.3, 4.0]	0.584	0.584	0.589
2	[1.1, 1.7]	0.196	0.197	0.196	[0.5, 3.5]	0.376	0.426	0.279
3	[1.4, 2.0]	0.106	0.126	0.103	[1.3, 3.6]	0.233	0.234	0.232
4	[1.8, 2.2]	0.085	0.085	0.085	[2.0, 3.5]	0.149	0.149	0.148
5	[1.3, 1.8]	0.070	0.071	0.069	[2.5, 3.5]	0.108	0.107	0.108

except for VKEW with $k = 2$. Comparing Tables 3 and 4 with Table 5, the big difference is that, for all k , VKIW outperforms VKEW. Moreover, for the inclusive patch, VKIW performs better than VKI. However, this is not true for the exclusive patch, where we see VKE has better convergence factors than VKEW.

4.1.3 | Optimized weights

From the above results, we see that LFA provides a good prediction for the actual two-grid performance, especially for the periodic problem. We also see that using geometric weights can improve performance. Motivated by this, we now consider whether using different weights for each different type of DoF within the relaxation scheme can improve performance. In this subsection, we apply LFA to optimize such weights. Here, we consider a preconditioned Richardson iteration, with corresponding two-grid error propagation operator

$$E_R = (I - \omega_2 M_h^{-1} K_h)^{v_2} \mathcal{M}^{\text{CGC}} (I - \omega_1 M_h^{-1} K_h)^{v_1}. \quad (20)$$

Our target is to optimize the corresponding convergence factor, ρ , by brute-force search or using other optimization algorithms. We also consider the effect of using different pre- and post-relaxation weights in (20).

Table 6 shows results for the $P_2 - P_1$ discretization when optimizing only the outer parameters in the Richardson relaxation. We use brute-force search with sampling points taken in steps of 0.02 on the interval $[0, 1]$ for $v_1 + v_2 = 1$. For $v_1 + v_2 = 2$, we use sampling points for ω_1 and ω_2 taken in steps of 0.02 on the intervals $[0, 0.5]$ and $[0.5, 0.9]$, respectively, to find the optimal results. Note that these intervals were selected based on results from a coarse sampling of wider intervals. We note that using $v_1 + v_2 = 1$ seems to be more efficient than using $v_1 + v_2 = 2$, except for the case of VKI, even when using two different weights for the pre- and post-relaxation parameters. We note that using different pre- and post-relaxation parameters gives notable improvements for VKE and VKI, but at best marginal gains for VKIW and VKEW.

Next, we consider fixing $\omega_1 = \omega_2 = 1$ in (20) and using three different weights for D_i : d_1 for N -type velocity DoFs, d_2 for X -, Y -, and C -type velocity DoFs, and d_3 for the pressure. We make use of a robust optimization algorithm designed for LFA optimization⁴⁷ to find the optimal parameters, rather than brute force searches. For the optimal parameters, we truncate the results obtained by the robust optimization to two digits, noting that the performance is not overly sensitive to this truncation. We first optimise for a single relaxation sweep, that is, $v_1 + v_2 = 1$. Table 7 shows that, in this setting, Vanka inclusive achieves a convergence factor of 0.581, while Vanka exclusive has a better convergence factor, 0.456. Both of these are significantly better than the corresponding results for VKI and VKE from Table 6, but only slightly better than VKIW and VKEW. Then, we optimise for the case of $v_1 + v_2 = 2$, showing that there is no significant improvement compared with a single relaxation. Comparing Tables 6 and 7 suggests that optimizing weights in D_i obtains better performance than doing so for the outer weights, although we note that nonsymmetric weighting of VKE in Table 6 outperforms the symmetric results in Table 7.

In order to see whether using more weights for different types of DoFs can improve the performance of Vanka relaxation, we consider fixing $\omega_1 = \omega_2 = 1$ and using four weights, d_1, d_2, d_3, d_4 , for the N -, X -, Y -, and C -type velocity DoFs, respectively, and one weight, d_5 , for the pressure in D_i . We again use the robust optimization algorithm.⁴⁷ Similarly, we first consider a single relaxation. The optimal weights and corresponding LFA predictions are presented in Table 8, showing that VKE achieves better performance than VKI. Then, we optimise with $v_1 + v_2 = 2$. We achieve a convergence factor of 0.415 for Vanka inclusive and 0.408 for Vanka exclusive, which are only slightly better than results using three weights. Table 8 suggests that a single relaxation is again more efficient for VKI and VKE, especially for the case of VKE. All in all, comparing Table 7 with Table 8 shows that using three weights for D_i is enough to obtain near-optimal performance. It is not necessary to use five weights.

TABLE 6 Two-grid LFA predictions, $\rho^{(\nu_1, \nu_2)}$, for Richardson relaxation optimizing outer weights for the $P_2 - P_1$ discretization.

Method	ω_{opt}	$\rho^{(1,0)}$	$(\omega_{1,\text{opt}}, \omega_{2,\text{opt}})$	$\rho^{(1,1)}$
VKI	0.24	0.819	(0.14, 0.50)	0.556
VKIW	0.78	0.587	(0.16, 0.84)	0.507
VKE	0.36	0.669	(0.22, 0.56)	0.356
VKEW	0.68	0.574	(0.00, 0.68)	0.574

TABLE 7 Two-grid LFA predictions for Richardson relaxation for the $P_2 - P_1$ discretization with three weights in D_i .

Method	$d_{1,\text{opt}}$	$d_{2,\text{opt}}$	$d_{3,\text{opt}}$	ρ
VKI ($\nu_1 + \nu_2 = 1$)	0.19	0.22	0.71	0.581
VKE ($\nu_1 + \nu_2 = 1$)	0.54	0.26	0.68	0.456
VKI ($\nu_1 + \nu_2 = 2$)	0.22	0.29	0.47	0.436
VKE ($\nu_1 + \nu_2 = 2$)	0.39	0.29	0.37	0.406

TABLE 8 Two-grid LFA predictions for Richardson relaxation for the $P_2 - P_1$ discretization with five weights in D_i .

Method	$d_{1,\text{opt}}$	$d_{2,\text{opt}}$	$d_{3,\text{opt}}$	$d_{4,\text{opt}}$	$d_{5,\text{opt}}$	ρ
VKI ($\nu_1 + \nu_2 = 1$)	0.19	0.21	0.17	0.35	0.74	0.571
VKE ($\nu_1 + \nu_2 = 1$)	0.49	0.25	0.24	0.30	0.68	0.452
VKI ($\nu_1 + \nu_2 = 2$)	0.22	0.28	0.28	0.30	0.51	0.415
VKE ($\nu_1 + \nu_2 = 2$)	0.43	0.33	0.30	0.32	0.36	0.408

4.1.4 | Sensitivity of convergence factors

Here, we present LFA results to show the sensitivity of performance to parameter choice for Richardson relaxation with VKI, VKIW, VKE and VKEW. In Figure 9, we show results for a single Richardson relaxation for Vanka inclusive and Vanka exclusive, sampling ω in steps of 0.02 on the interval $[0, 1]$. Figure 9 shows that it is better to underestimate the optimal parameter than to overestimate it. Similar behaviour is seen in other works. Adler et al.¹² explored different types of Vanka as a preconditioner for GMRES for magnetohydrodynamics, showing the same preference for underestimation of the optimal parameter. In the application of Vanka relaxation for the Stokes equations with an $H(\text{div})$ conforming discretization,⁴ even when using different weights for the velocity and pressure DoFs, it also appears better to underestimate the optimal parameters. We note that for both Vanka-inclusive and Vanka-exclusive with natural weights, convergence is observed for a wider range of Richardson weights than for Vanka-inclusive and Vanka-exclusive.

In Figures 10 and 11, we present the LFA convergence factor as function of ω_1 and ω_2 , sampling in steps of 0.05 on the interval $[0, 1]$, for Richardson relaxation with $\nu_1 + \nu_2 = 2$. We see similar behaviour, that performance degrades rapidly for weights that are “too large”. For Vanka-inclusive, the case with no weights is more sensitive to the outer parameters, while the opposite is seen for Vanka-exclusive.

4.2 | Numerical results for the $Q_2 - Q_1$ discretization

Similarly to the case of the $P_2 - P_1$ discretization, we consider Chebyshev-Vanka relaxation and preconditioned Richardson relaxation within monolithic multigrid methods for the Stokes equations for the $Q_2 - Q_1$ discretization. Here, all of the optimal parameters are obtained by using the robust optimization algorithm,⁴⁷ and we compare the LFA predictions with performance observed for the discretization with periodic boundary conditions with $h = \frac{1}{40}$. We remark that the measured convergence factors with Dirichlet boundary conditions also match well with the LFA predictions. For the optimal parameters, we truncate the results obtained by the robust optimization to two digits, noting that the performance is not sensitive to this truncation.

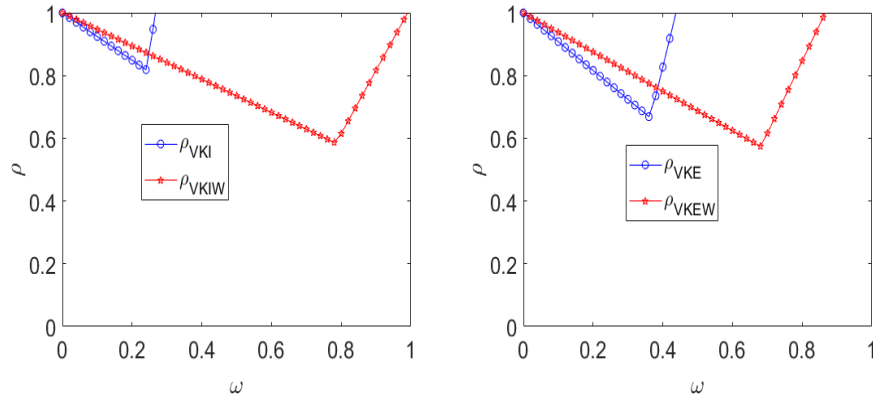


FIGURE 9 Two-grid LFA convergence factor as a function of ω for Richardson relaxation with $\nu_1 + \nu_2 = 1$. Left: Vanka-inclusive and Vanka-inclusive with natural weights. Right: Vanka-exclusive and Vanka-exclusive with natural weights.

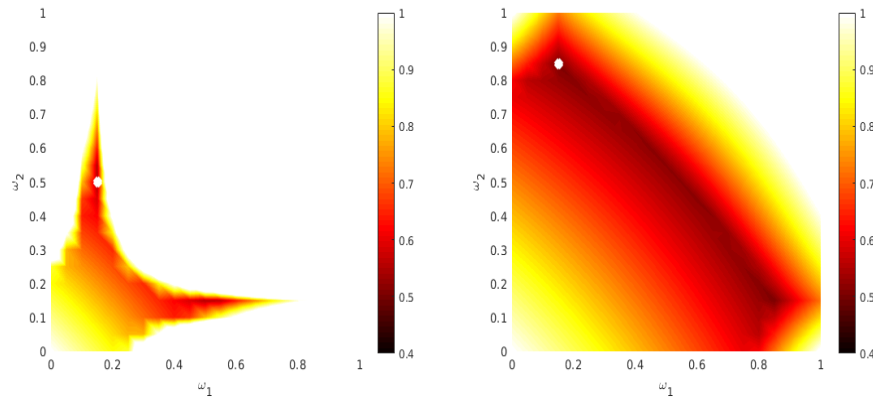


FIGURE 10 Two-grid LFA convergence factor as a function of ω_1 and ω_2 for Richardson relaxation with $\nu_1 + \nu_2 = 2$. The white circle marks the optimal point. Left: Vanka-inclusive. Right: Vanka-inclusive with natural weights.

Tables 9 and 10 present the measured convergence for periodic boundary conditions versus the LFA predictions for different k and the corresponding optimal intervals for Chebyshev-Vanka relaxation with no weights and natural weights, respectively. Similarly to the case of the $P_2 - P_1$ discretizations, we see that the optimal pair of $[\alpha, \beta]$ is not unique in some cases. We break such ties arbitrarily. We see good agreement between the LFA predictions and the multigrid performance, except for VKI with $k = 5$ and VKEW with $k = 2$. For the former case, the per iteration convergence factor oscillates in the range from 0.12 to 0.22, averaging close to that predicted by LFA. For the latter, more variation is seen in the per-cycle convergence factors, between 0.07 and 1.19, but the long-term average still approaches that given by LFA. For these cases, we present averaged convergence over the final five iterations. Comparing Tables 9 and 10 shows that the patches with natural weights outperform those with no weights, in some cases by a large margin. An interesting observation from these tables, particularly Table 10, is that the optimization has a natural preference for giving very small intervals. This would normally be a cause for concern, but clearly leads to excellent behaviour in this setting.

Table 11 gives results for the $Q_2 - Q_1$ discretization when optimizing only the outer parameter as in Table 6. While using 2 weights is effective for VKI and VKE, better efficiency is seen for a single sweep with natural weights. We also consider fixing $\omega_1 = \omega_2 = 1$ in (20) and optimizing the inner weights. Table 12 shows the optimal results for preconditioned Richardson relaxation with three parameters. Note that, as above, optimizing five weights does not improve the performance; thus, we omit the results here. Optimizing three weights obtains significantly better results than above for VKI, but shows little improvement when increasing the number of relaxation sweeps. As above, optimizing three weights offers some improvement over natural weights, but not enough to suggest further optimization is worthwhile.

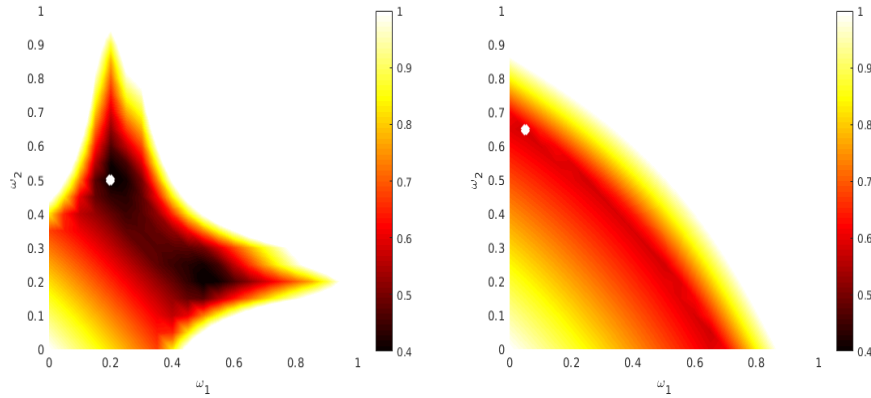


FIGURE 11 Two-grid LFA convergence factor as a function of ω_1 and ω_2 for Richardson relaxation with $v_1 + v_2 = 2$. The white circle marks the optimal points. Left: Vanka-exclusive. Right: Vanka-exclusive with natural weights.

TABLE 9 Two-grid LFA predictions for Chebyshev Vanka relaxation and two-grid performance with periodic boundary conditions ($\hat{\rho}$) for the $Q_2 - Q_1$ discretization. Optimal intervals for different k with no weights. $h = \frac{1}{40}$. An alternating convergence pattern was observed, so the reported convergence factor is averaged over the final five iterations before convergence (denoted *).

k	$[\alpha, \beta]_{\text{VKI}}$	ρ_{VKI}	$\hat{\rho}_{\text{VKI}}$	$[\alpha, \beta]_{\text{VKE}}$	ρ_{VKE}	$\hat{\rho}_{\text{VKE}}$
1	[4.61, 4.81]	0.866	0.864	[3.40, 3.49]	0.770	0.769
2	[4.72, 4.73]	0.752	0.752	[0.96, 5.99]	0.506	0.509
3	[3.66, 5.82]	0.642	0.635	[0.79, 6.18]	0.326	0.327
4	[0.39, 9.14]	0.203	0.201	[0.91, 6.03]	0.262	0.263
5	[0.37, 11.42]	0.162	0.166*	[3.29, 3.67]	0.278	0.277

TABLE 10 Two-grid LFA predictions for Chebyshev Vanka relaxation and two-grid performance with periodic boundary conditions ($\hat{\rho}$) for the $Q_2 - Q_1$ discretization. Optimal intervals for different k with natural weights. $h = \frac{1}{40}$. An alternating convergence pattern was observed, so the reported convergence factor is averaged over the final five iterations before convergence (denoted *).

k	$[\alpha, \beta]_{\text{VKIW}}$	ρ_{VKIW}	$\hat{\rho}_{\text{VKIW}}$	$[\alpha, \beta]_{\text{VKEW}}$	ρ_{VKEW}	$\hat{\rho}_{\text{VKEW}}$
1	[0.15, 2.95]	0.637	0.636	[1.32, 3.51]	0.681	0.683
2	[0.71, 1.97]	0.288	0.290	[1.50, 1.54]	0.271	0.265*
3	[0.90, 1.42]	0.153	0.161	[1.93, 1.99]	0.234	0.241
4	[1.23, 1.24]	0.097	0.098	[2.38, 2.39]	0.217	0.221
5	[1.17, 1.40]	0.071	0.072	[1.57, 2.41]	0.129	0.128

4.3 | Comparing cost and performance

4.3.1 | Cost of relaxation for the $P_2 - P_1$ discretization

All schemes have the same cost for computing the initial residual. The P_2 Laplacian, A , contains four types of stencils, that is, a 9-point stencil for N -type points, and 5-point stencils for X -, Y - and C -type points, and B_x and B_y have 10-point stencils. Away from boundaries, we can naturally associate each DoF with a node, to see that a mesh with n nodes also has about n of each type of edge DoF. So, the cost of a single residual evaluation on a mesh with n nodes is (roughly) that of $(9 + 3 \cdot 5)n \cdot 2 + 10 \cdot n \cdot 4 = 88n$ multiply-add operations, coming from the 6 nonzero blocks in the matrix.

For the $P_2 - P_1$ discretization, the remaining cost is that of solving a small problem, $K_i x_i = b_i$, in each patch. Here, we use LU decomposition to solve these subproblems. Assume that the LU decomposition is precomputed, as this can be done once

TABLE 11 Two-grid LFA predictions, $\rho^{(v_1, v_2)}$, for Richardson relaxation optimizing outer weights for the $Q_2 - Q_1$ discretization.

Method	ω_{opt}	$\rho^{(1,0)}$	$(\omega_{1,\text{opt}}, \omega_{2,\text{opt}})$	$\rho^{(1,1)}$
VKI	0.21	0.931	(0.13, 0.60)	0.809
VKIW	0.92	0.712	(0.65, 0.65)	0.637
VKE	0.29	0.878	(0.76, 0.17)	0.639
VKEW	0.73	0.697	(0.41, 0.41)	0.684

TABLE 12 Two-grid LFA predictions for Richardson relaxation for the $Q_2 - Q_1$ discretization with three weights in D_i .

Method	$d_{1,\text{opt}}$	$d_{2,\text{opt}}$	$d_{3,\text{opt}}$	ρ
VKI ($v_1 + v_2 = 1$)	0.10	0.13	1.00	0.695
VKE ($v_1 + v_2 = 1$)	0.88	0.20	0.84	0.648
VKI ($v_1 + v_2 = 2$)	0.15	0.09	0.79	0.583
VKE ($v_1 + v_2 = 2$)	0.18	0.22	0.48	0.646

TABLE 13 The number (#) of nonzero elements of L and U ($LU = K_i$) for Vanka-inclusive and Vanka-exclusive patches for the $P_2 - P_1$ and $Q_2 - Q_1$ discretizations.

patch #	$P_2 - P_1$		$Q_2 - Q_1$	
	Ξ_{VKI}	Ξ_{VKE}	Ξ_{VKI}	Ξ_{VKE}
L	284	115	617	335
U	282	115	617	337
Total	566	230	1234	672

per patch and used for all of the solves over that patch. As in Table 2, for VKI and VKIW, the size of the patch problem is $2(7 + 4 + 4 + 4) + 1 = 39$. For VKE and VKEW, it is $2(1 + 2 + 2 + 4) + 1 = 27$. Note that, similarly to K , K_i is a block (sparse) matrix, and its LU factors will retain some sparsity as well. Thus, the cost of solving the sparse systems with L or U will require a number of multiply-add operations equal to the number of nonzero entries in L or U . Table 13 presents these numbers, based on direct calculation of the factorizations. For VKI and VKIW, the cost of applying the inverses of L and U is 566 multiply-add operations. For the whole system, we need to solve roughly n subproblems, giving a total cost of $566n$. Similarly, it costs $230n$ multiply-add operations for VKE and VKEW. For the approaches with natural weights, we need an additional scaling for each subproblem. Thus, there will be an additional cost of $39n$ and $27n$ for VKIW and VKEW, respectively.

Accumulating the costs of a residual evaluation with these, we have total costs of $88n + 566n = 654n$ multiply-add operations per sweep of VKI, $88n + 230n = 318n$ multiply-add operations per sweep of VKE, $654n + 39n = 693n$ multiply-add operations per sweep of VKIW, and $318n + 27n = 345n$ multiply-add operations per sweep of VKEW. To compare these costs, we omit the cost of the coarse-grid correction and only consider the cost of the relaxation scheme. We denote the above cost as W_s , which corresponds to $k = 1$ and $v_1 + v_2 = 1$. Comparing efficiencies can now be easily done by appropriately weighting either measured or predicted convergence factors relative to their work (here, we use the predicted convergence factors): if one iteration costs W times that of another, and yields a convergence factor of ρ_1 , then we can easily compare $\rho_1^{1/W}$ directly to the second convergence factor, ρ_2 , to see if the effective error reduction achieved by the first algorithm in an equal amount of work to the second is better or worse than that achieved by the second. Here, we compare the efficiency relative to VKEW.

Next, using the data presented above, we find the most effective parameters for each of VKI, VKE, VKIW and VKEW, and compare their costs. From Tables 3 and 4, we see the most effective choice for VKI is $k = 3$ giving $\rho = 0.120$, while, for VKE, it is $k = 1$ giving $\rho = 0.475$. Note, however, that a more efficient set of parameters for VKE is found in Table 6, giving a convergence factor of 0.356 per iteration. From Table 5, the most effective choice for VKIW is $k = 2$ giving $\rho = 0.196$, and $k = 1$ giving $\rho = 0.584$ for VKEW. Here, optimizing with more weights, as in Tables 7 and 8, was more effective, and we consider

TABLE 14 Comparing cost and performance for the $P_2 - P_1$ discretization.

	VKI	VKE	VKIW	VKEW
$W_s (k = 1, \nu_1 + \nu_2 = 1)$	654n	318n	693n	345n
Most Effective $(k, \nu_1 + \nu_2)$	(3, 2)	(1, 2)	(1, 1)	(1, 1)
ρ	0.120	0.356	0.571	0.452
$W_t = k \cdot (\nu_1 + \nu_2) \cdot W_s$				
W_t	3924n	636n	693n	345n
Relative Efficiency	0.830	0.571	0.757	0.452

TABLE 15 Comparing cost and performance for the $Q_2 - Q_1$ discretization.

	VKI	VKE	VKIW	VKEW
$W_s (k = 1, \nu_1 + \nu_2 = 1)$	1338n	776n	1389n	811n
Most Effective $(k, \nu_1 + \nu_2)$	(4, 2)	(1, 2)	(1, 1)	(1, 1)
ρ	0.203	0.639	0.695	0.648
$W_t = k \cdot (\nu_1 + \nu_2) \cdot W_s$				
W_t	10704n	1552n	1389n	811n
Relative Efficiency	0.886	0.791	0.809	0.648

the best results with a non-trivial scaling matrix, D_i , in place of the geometric weights, giving 0.571 for VKIW and 0.452 for VKEW. Now, we can calculate the efficiency for each relaxation scheme relative to its total cost, $W_t = k \cdot (\nu_1 + \nu_2) \cdot W_s$, where W_s denotes the cost of a single relaxation. Table 14 details the cost-effectiveness for each scheme for the $P_2 - P_1$ discretization, showing that VKEW offers the most efficient relaxation scheme. In particular, this shows that the substantially smaller cost per iteration of the exclusive patches offers greater efficiency, despite the improved convergence when using inclusive patches.

4.3.2 | Cost of relaxation for the $Q_2 - Q_1$ discretization

The Q_2 Laplacian, A , contains four types of stencils, a 25-point stencil for N -type points, 15-point stencils for X -, and Y - DoFs and a 9-point stencil for C -type points, while B_x and B_y have 12-point stencils. So, the cost of a single residual evaluation on a mesh with n nodes is (roughly) that of $(25 + 2 \cdot 15 + 9)n \cdot 2 + 12 \cdot n \cdot 4 = 104n$ multiply-add operations, coming from the 6 nonzero blocks in the matrix.

For the $Q_2 - Q_1$ approximation with additive Vanka-type relaxation, there is little difference in the cost calculation compared with that of the $P_2 - P_1$ discretization. Here, we again use the LU decomposition of the patch matrices, K_i , and assume the LU decomposition is done. For VKI, the cost of applying the inverses of L and U is 1234 multiply-add operations per block, see Table 13. Thus, the cost for a full sweep is 1234n multiply-add operations. Similarly, it costs 672n multiply-add operations per sweep of VKE. For the approaches with natural weights, there will be an additional cost of 51n and 35n for VKIW and VKEW, respectively, for these scaling operations. Accumulating the costs of a residual evaluation with these, we have total costs of $104n + 1234n = 1338n$ multiply-add operations per sweep of VKI, $104n + 672n = 776n$ multiply-add operations per sweep of VKE, $1338 + 51n = 1389n$ multiply-add operations per sweep of VKIW, and $776n + 35n = 811n$ multiply-add operations per sweep of VKEW.

From Tables 9 and 10, we see the most effective choice for VKI is $k = 4$ giving $\rho = 0.203$, while, for VKE, it is $k = 3$ giving $\rho = 0.326$. Note, however, that a more efficient set of parameters for VKE is found in Table 11, giving a convergence factor of 0.639 per iteration with $\nu_1 + \nu_2 = 2$. From Table 10, the most effective choice for VKIW is $k = 3$ giving $\rho = 0.153$, and $k = 2$ giving $\rho = 0.271$ for VKEW. Here, optimizing with more weights, as in Table 12, was more effective, and we consider the best results with a non-trivial scaling matrix, D_i , in place of the geometric weights, giving 0.695 for VKIW and 0.648 for VKEW with $\nu_1 + \nu_2 = 1$. Table 15 compares the efficiency relative to VKEW, showing that the most efficient choice is VKEW, the same as for the $P_2 - P_1$ discretization.

5 | CONCLUSIONS AND FUTURE WORK

We present a local Fourier analysis for a monolithic multigrid method based on overlapping additive Vanka-type relaxation for the Stokes equations. Two choices of patches for the overlapping schemes are discussed for the P_2-P_1 and Q_2-Q_1 discretizations. A general framework of LFA for additive Vanka relaxation is developed to help choose algorithmic parameters, which can be applied to other problems and to different discretizations. The LFA shows that using smaller patches can outperform relaxation using bigger patches due to the lower cost per sweep of relaxation. Moreover, to improve the performance, we use LFA to optimize the weights, yielding notable improvement. Numerical performance with periodic and Dirichlet boundary conditions validate the LFA predictions, showing that these Vanka relaxation schemes are robust to the different boundary conditions.

Extending Vanka relaxation for other types of problems is an interesting topic. We note that this LFA framework of additive Vanka relaxation has a limitation: since we need to know the patch first, selection of the patches is not readily optimized in this framework. Another interesting question is the use of other boundary conditions on the patches, such as are used in optimized Schwarz, which could also be tuned using LFA. Developing general-purpose LFA software for additive Vanka with automatic evaluation of patch choices and optimizing the weights are also topics for future work.

ACKNOWLEDGMENTS

The work of P. E. F. was supported by the Engineering and Physical Sciences Research Council [grant numbers EP/K030930/1 and EP/R029423/1]. The work of S. P. M. was partially supported by an NSERC Discovery Grant.

References

1. Benzi M, Golub GH, and Liesen J. Numerical solution of saddle point problems. *Acta Numerica*. 2005;**14**:1–137.
2. Wathen A, and Silvester D. Fast iterative solution of stabilised Stokes systems. Part I: Using simple diagonal preconditioners. *SIAM Journal on Numerical Analysis*. 1993;**30**(3):630–649.
3. Silvester D, and Wathen A. Fast iterative solution of stabilised Stokes systems part II: using general block preconditioners. *SIAM Journal on Numerical Analysis*. 1994;**31**(5):1352–1367.
4. Adler JH, Benson TR, and MacLachlan SP. Preconditioning a mass-conserving discontinuous Galerkin discretization of the Stokes equations. *Numerical Linear Algebra with Applications*. 2017;**24**(3):e2047.
5. Geenen T, M ur Rehman, MacLachlan SP, Segal G, Vuik C, A P van den Berg, et al. Scalable robust solvers for unstructured FE modeling applications; solving the Stokes equation for models with large, localized viscosity contrasts. *Geochemistry, Geophysics, Geosystems*. 2009;**10**(9).
6. Rudi J, Malossi ACI, Isaac T, Stadler G, Gurnis M, Staar PWJ, et al. An Extreme-scale Implicit Solver for Complex PDEs: Highly Heterogeneous Flow in Earth’s Mantle. In: *Proceedings of the International Conference for High Performance Computing, Networking, Storage and Analysis. SC ’15*. New York, NY, USA: ACM; 2015. p. 5:1–5:12. Available from: <http://doi.acm.org/10.1145/2807591.2807675>.
7. John V, and Tobiska L. Numerical performance of smoothers in coupled multigrid methods for the parallel solution of the incompressible Navier-Stokes equations. *International Journal For Numerical Methods In Fluids*. 2000 Jan;**33**(4):453–473.
8. Gmeiner B, Rde U, Stengel H, Waluga C, and Wohlmuth B. Performance and scalability of hierarchical hybrid multigrid solvers for Stokes systems. *SIAM Journal on Scientific Computing*. 2015;**37**(2):C143–C168.
9. Gmeiner B, Huber M, John L, Rde U, and Wohlmuth B. A quantitative performance study for Stokes solvers at the extreme scale. *J Comput Sci*. 2016;**17**(part 3):509–521. Available from: <https://doi.org/10.1016/j.jocs.2016.06.006>.
10. Niestegge A, and Witsch K. Analysis of a multigrid Stokes solver. *Applied Mathematics and Computation*. 1990;**35**(3):291–303.

11. Braess D, and Sarazin R. An efficient smoother for the Stokes problem. *Applied Numerical Mathematics*. 1997;**23**:3–20.
12. Adler JH, Benson TR, Cyr EC, MacLachlan SP, and Tuminaro RS. Monolithic multigrid methods for two-dimensional resistive magnetohydrodynamics. *SIAM Journal on Scientific Computing*. 2016;**38**(1):B1–B24.
13. Vanka SP. Block-implicit multigrid solution of Navier-Stokes equations in primitive variables. *Journal of Computational Physics*. 1986;**65**:138–158.
14. Wang M, and Chen L. Multigrid methods for the Stokes equations using distributive Gauss–Seidel relaxations based on the least squares commutator. *Journal of Scientific Computing*. 2013;**56**(2):409–431.
15. Chen L, Hu X, Wang M, and Xu J. A multigrid solver based on distributive smoother and residual overweighing for Oseen problems. *Numerical Mathematics: Theory, Methods and Applications*. 2015;**8**(02):237–252.
16. Adler JH, Emerson DB, MacLachlan SP, and Manteuffel TA. Constrained optimization for liquid crystal equilibria. *SIAM Journal on Scientific Computing*. 2016;**38**(1):B50–B76.
17. He Y, and MacLachlan SP. Local Fourier analysis of block-structured multigrid relaxation schemes for the Stokes equations. *Numerical Linear Algebra with Applications*. 2018;**25**(3)(3):e2147.
18. He Y, and MacLachlan SP. Local Fourier analysis for mixed finite-element methods for the Stokes equations. *Journal of Computational and Applied Mathematics*. 2019;**357**:161–183.
19. John V. Higher order finite element methods and multigrid solvers in a benchmark problem for the 3D Navier–Stokes equations. *International Journal for Numerical Methods in Fluids*. 2002;**40**(6):775–798.
20. John V, and Matthies G. Higher-order finite element discretizations in a benchmark problem for incompressible flows. *International Journal For Numerical Methods In Fluids*. 2001 Jan;**37**(8):885–903.
21. Manservigi S. Numerical analysis of Vanka-type solvers for steady Stokes and Navier–Stokes flows. *SIAM Journal on Numerical Analysis*. 2006;**44**(5):2025–2056.
22. Schöberl J, and Zulehner W. On Schwarz-type smoothers for saddle point problems. *Numerische Mathematik*. 2003;**95**(2):377–399.
23. Rodrigo C, Gaspar FJ, and Lisbona FJ. On a local Fourier analysis for overlapping block smoothers on triangular grids. *Applied Numerical Mathematics*. 2016;**105**:96–111.
24. MacLachlan SP, and Oosterlee CW. Local Fourier analysis for multigrid with overlapping smoothers applied to systems of PDEs. *Numerical Linear Algebra with Applications*. 2011;**18**:751–774.
25. de la Riva ÁP, Rodrigo C, and Gaspar FJ. An efficient multigrid solver for isogeometric analysis. *arXiv preprint arXiv:180605848*. 2018;.
26. Sivaloganathan S. The use of local mode analysis in the design and comparison of multigrid methods. *Computer Physics Communications*. 1991;**65**(1-3):246–252.
27. Molenaar J. A two-grid analysis of the combination of mixed finite elements and Vanka-type relaxation. In: *Multigrid methods III*. Springer; 1991. p. 313–323.
28. Boonen T, Van Lent J, and Vandewalle S. Local Fourier analysis of multigrid for the curl-curl equation. *SIAM Journal on Scientific Computing*. 2008;**30**(4):1730–1755.
29. Rathgeber F, Ham DA, Mitchell L, Lange M, Luporini F, McRae AT, et al. Firedrake: automating the finite element method by composing abstractions. *ACM Transactions on Mathematical Software (TOMS)*. 2017;**43**(3):24.
30. Balay S, Abhyankar S, Adams M, Brown J, Brune P, Buschelman K, et al.. 2018. *PETSc Users Manual: Revision 3.10*. . Argonne National Lab.(ANL), Argonne, IL (United States).

31. Kirby RC, and Mitchell L. Solver composition across the PDE/linear algebra barrier. *SIAM Journal on Scientific Computing*. 2018;**40**(1):C76–C98.
32. Elman HC, Silvester DJ, and Wathen AJ. Finite elements and fast iterative solvers with applications in incompressible fluid dynamics. 2nd ed. *Numerical Mathematics and Scientific Computation*. Oxford University Press, Oxford; 2014.
33. Brenner SC, and Scott LR. The mathematical theory of finite element methods. vol. 15 of *Texts in Applied Mathematics*. 3rd ed. Springer, New York; 2008.
34. Brezzi F, and Douglas J. Stabilized mixed methods for the Stokes problem. *Numerische Mathematik*. 1988;**53**(1):225–235.
35. Dohrmann CR, and Bochev PB. A stabilized finite element method for the Stokes problem based on polynomial pressure projections. *International Journal for Numerical Methods in Fluids*. 2004;**46**(2):183–201.
36. Limache A, Idelsohn S, Rossi R, and Oñate E. The violation of objectivity in Laplace formulations of the Navier–Stokes equations. *International Journal for Numerical Methods in Fluids*. 2007;**54**(6-8):639–664.
37. Trottenberg U, Oosterlee CW, and Schüller A. *Multigrid*. Academic Press, Inc., San Diego, CA; 2001. With contributions by A. Brandt, P. Oswald and K. Stüben.
38. Stüben K, and Trottenberg U. Multigrid methods: Fundamental algorithms, model problem analysis and applications. In: *Multigrid methods*. Springer; 1982. p. 1–176.
39. Wesseling P. An introduction to multigrid methods. *Pure and Applied Mathematics (New York)*. John Wiley & Sons, Ltd., Chichester; 1992.
40. Saad Y. *Iterative methods for sparse linear systems*. vol. 82. SIAM; 2003.
41. Wienands R, and Joppich W. *Practical Fourier analysis for multigrid methods*. CRC press; 2004.
42. He Y, and MacLachlan SP. Two-level Fourier analysis of multigrid for higher-order finite-element methods. revised. 2019;.
43. Logg A, Mardal KA, Wells GN, et al. *Automated Solution of Differential Equations by the Finite Element Method*. Springer; 2012.
44. Alnæs MS, Blechta J, Hake J, Johansson A, Kehlet B, Logg A, et al. The FEniCS Project Version 1.5. *Archive of Numerical Software*. 2015;**3**(100).
45. Rodrigo C, Sanz F, Gaspar FJ, and Lisbona FJ. Local Fourier analysis for edge-based discretizations on triangular grids. *Numerical Mathematics: Theory, Methods and Applications*. 2015;**8**(1):78–96.
46. Stevenson RP. *On the validity of local mode analysis of multi-grid methods*. Utrecht, The Netherlands: Utrecht University; 1990.
47. Brown J, He Y, MacLachlan SP, Menickelly M, and Wild S. Tuning multigrid methods with robust optimization; 2019.

